Prospects for exotic $h \to 4\tau$ decays in single and di-Higgs boson production at the LHC and future hadron colliders

Amit Adhikary,[1,2,*] Shankha Banerjee,[3,†] Rahool Kumar Barman,[4,‡] Brian Batell,[5,§] Biplob Bhattacherjee,[2,‖] Camellia Bose,[2,¶] Zhuoni Qian,[6,**] and Michael Spannowsky[7,††]

[1]*Institute of Theoretical Physics, Faculty of Physics, University of Warsaw, Pasteura 5, PL 02-093, Warsaw, Poland*
[2]*Centre for High Energy Physics, Indian Institute of Science, Bangalore 560012, India*
[3]*CERN, Theoretical Physics Department, CH-1211 Geneva 23, Switzerland*
[4]*Department of Physics, Oklahoma State University, Stillwater, Oklahoma 74078, USA*
[5]*Pittsburgh Particle Physics, Astrophysics, and Cosmology Center, Department of Physics and Astronomy, University of Pittsburgh, Pittsburgh 15260, USA*
[6]*Hangzhou Normal University, Hangzhou, Zhejiang 311121, China*
[7]*Institute for Particle Physics Phenomenology, Durham University, South Road, Durham DH1 3LE, United Kingdom*

(Received 14 December 2022; accepted 6 February 2024; published 7 March 2024)

We study the prospects for observing exotic decays of the Standard Model Higgs boson h into light beyond the Standard Model scalars a with mass $m_a \lesssim m_h/2$ in the single Higgs and Higgs pair production channels at the high luminosity run of the Large Hadron Collider (HL-LHC). Discovery prospects for single Higgs production in the gluon-gluon fusion and vector boson fusion modes with the Higgs boson decaying via the exotic mode $h \to aa \to 4\tau$ are analyzed at the HL-LHC. The projected sensitivity for exotic Higgs decays in the nonresonant Higgs pair production channel $pp \to hh \to (h \to b\bar{b})(h \to aa \to 4\tau) \to 2b4\tau$ at the HL-LHC and a future $\sqrt{s} = 100$ TeV hadron collider (FCC-hh) are also estimated. Furthermore, we study HL-LHC's potential reach for the Higgs-strahlung process in the $2b4\tau$ channel, taking into account the contamination from nonresonant Higgs pair production. Finally, the potential reach for resonant Higgs pair production in the $2b4\tau$ channel at the HL-LHC is also explored for several choices of $\{m_H, m_a\}$. Our studies suggest that significant improvements over existing bounds are achievable in several production channels, motivating new dedicated searches for $h \to aa \to 4\tau$ at the HL-LHC and future colliders.

DOI: 10.1103/PhysRevD.109.055008

I. INTRODUCTION

Despite bearing a high degree of consistency with the Standard Model (SM) predictions, the current Higgs measurements still allow significant room for the Higgs boson to have nonstandard decays. The ATLAS collaboration has analyzed the $\sqrt{s} = 13$ TeV data collected at $\mathcal{L} = 139$ fb^{-1} and has derived upper limits on the branching ratios of the Higgs boson to undetected ~19% and invisible particles ~11%, at 95% CL, through combined measurements of single Higgs boson production in gluon-gluon fusion (ggF), vector boson fusion (VBF), Vh, and $t\bar{t}h$ modes, and decay in $h \to b\bar{b}, \gamma\gamma, ZZ^\star, W^+W^-, \tau^+\tau^-, \mu^+\mu^-$ channels [1]. Thus, nonstandard or exotic decays of the Higgs boson are still allowed with appreciable branching rates and remain a well-motivated and exciting opportunity to probe new physics [2,3]. Given the generic expectation of novel event topologies and decay kinematics in a variety of well-motivated exotic Higgs decay channels, dedicated search strategies are required to fully discern their discovery potential.

Exotic decays of the Higgs boson can be realized in various beyond the SM (BSM) frameworks. One typical example is the Higgs portal scenario where the Higgs field weakly couples to a light hidden sector [4–13]. Similarly, BSM theories with extended Higgs sectors, including supersymmetric extensions, often predict exotic Higgs decays. A widely studied example from the latter category

*amit.adhikary@fuw.edu.pl
†shankha.banerjee@cern.ch
‡rahool.barman@okstate.edu
§batell@pitt.edu
‖biplob@iisc.ac.in
¶camelliabose@iisc.ac.in
**zhuoniqian@hznu.edu.cn
††michael.spannowsky@durham.ac.uk

is the next-to-minimal supersymmetric SM where the Higgs sector consists of two Higgs doublets and a singlet [14–16]. Here, the lightest (pseudo)scalar Higgs can be singletlike with mass $\leq m_h/2$, leading to exotic decays of the SM-like Higgs boson. The ATLAS and CMS collaborations have explored exotic Higgs decays in single Higgs production channels viz., $pp \to h \to aa \to X, X = 4b$ [17,18], $2b2\tau$ [19], $2b2\mu$ [20–22], 4μ [23,24], $2\mu2\tau$ [25–29], 4γ [30], and $2\gamma2j$ ($j =$ jets) [31]. Here, a is a new spin-0 boson that couples with the SM Higgs boson h with mass $m_a \leq m_h/2$ such that it is kinematically possible for h to decay via $h \to aa$. These analyses assume several extensions of the two Higgs doublet model (2HDM) while maintaining SM-like Higgs production cross sections such as Refs. [19,21,27,28] by CMS and Refs. [17,18,20] by ATLAS collaboration, where type III 2HDM+S model have been incorporated. Assuming SM production cross section, upper limits have been derived on $\mathrm{Br}(h \to aa \to X)$ at 95% CL, as presented in Table I.

In this paper, we study the prospects for probing the exotic Higgs decay

$$h \to aa \to 4\tau \tag{1.1}$$

at the high luminosity run of the Large Hadron Collider (HL-LHC) and a future 100 TeV hadron collider (FCC-hh) from several directions. This channel is particularly well motivated for a couple of reasons. From a theoretical perspective, if a has preferential couplings to leptons with an interaction strength that is proportional to the lepton mass, as is often the case, then it is natural to expect $a \to \tau\bar{\tau}$ to dominate over other possible a decay channels. For simplicity, we will take a phenomenological approach in this work, assuming that a decays solely via $a \to \tau\bar{\tau}$ and the branching ratios to any other possible channels are negligible. Besides being theoretically motivated, the current experimental bounds on the exotic decay branching ratio $\mathrm{Br}(h \to aa \to 4\tau)$ are relatively weak, particularly for m_a larger than about 15 GeV, allowing for the possibility of large event rates depending on the Higgs production channel under consideration. Let us summarize the current experimental status for this channel.

A CMS search in the $h \to aa \to 4\tau/2\mu2\tau$ mode has placed 95% CL upper limits on $\mathrm{Br}(h \to aa \to 4\tau)$ in the low m_a range of 4–15 GeV [26]. The limits vary from 0.23 at $m_a = 4$ GeV to 0.16 at $m_a = 15$ GeV, being strongest at $m_a = 9$ GeV with a limit of 0.022. On the other hand, for heavier exotic scalars, $\mathrm{Br}(h \to aa \to 4\tau)$ is only weakly constrained by existing experimental analyses [2,33,34]. Upper limits on $\mathrm{Br}(h \to aa \to 4\tau)$ in the $m_a \geq 15$ GeV regime has been derived in a recent ATLAS search which focuses on the $gg \to h \to aa \to 4\tau$ mode, considering the 4τ final state with two same-sign (SS) charged leptons and two SS τ jets [32]. This search excludes $\mathrm{Br}(h \to aa \to 4\tau)$ up to 0.3 (0.1) for $m_a = 15(60)$ GeV in the SS $\mu^{\pm}\mu^{\pm}+$ SS τ jets channel at 95% CL.

If the exotic decay (1.1) is present, then it is natural to expect it to first be detected in the single Higgs production channels with the largest rate. Therefore, our first investigations in this work focus on the discovery prospects for $h \to aa \to 4\tau$ in the ggF and VBF induced single Higgs production channels at the HL-LHC.

Observing Higgs boson pair production, and in turn measuring the Higgs self-coupling and studying the scalar potential, is one of the major goals of the HL-LHC and future colliders. New physics can significantly impact the discovery prospects of the di-Higgs channel.

As is well-known, the rates of di-Higgs production can be enhanced in the presence of heavy resonances, as well as by new particles in the loops. Besides new physics that modifies di-Higgs production, it is also worthwhile to consider the impact of exotic Higgs decays in Higgs pair production.

TABLE I. Model-independent upper limits at 95% CL on the branching ratio of Higgs boson to pseudoscalars with a further decay into various four-particle final states.

		95% CL upper limit on	
Channel (X)	Mass of a, m_a (GeV)	$\sigma \times \mathrm{Br}(h \to aa \to X)$ (fb)	$\mathrm{Br}(h \to aa \to X)$
$b\bar{b}b\bar{b}$ [17,18]	[20, 60]	[3000, 1300]	⋯
$2b2\tau$ [19]	[15, 60]	⋯	[0.03, 0.12]
$2b2\mu$ [20]	[20, 60]	⋯	$(1.2\text{–}8.4) \times 10^{-4}$
$2b2\mu$ [21]	[20, 62.5]	⋯	$(1\text{–}7) \times 10^{-4}$
$2b2\mu$ [22]	[16, 62]	⋯	$(0.2\text{–}4) \times 10^{-4}$
4μ [23,24]	[0.25, 8.5]	[0.15, 0.39]	⋯
4τ [32]	[15, 60]	⋯	[0.30, 0.10]
$2\mu2\tau$ [25]	[3.6, 21]	⋯	upto 1.5×10^{-4}
$4\tau/2\mu2\tau$ [26]	[4,15] (9)	⋯	[0.23, 0.16](0.022)
$2\mu2\tau$ [27–29]	[15, 62.5]	⋯	upto 1.2×10^{-4}
4γ [30]	[10, 62]	$[3 \times 10^{-4}, 4 \times 10^{-4}] \times \sigma_{\mathrm{SM}}$	⋯
$2\gamma2j$ [31]	[20, 60]	[3100, 9000]	⋯

Such a case where one of the Higgs decays to a pair of invisible particles was first studied in Ref. [35] and later in Refs. [36,37]. Probing di-Higgs production in the SM is extremely challenging, with the projected constraints on the Higgs trilinear self-coupling at the FCC-hh being ∼5% [38]. Thus additional final states could in principle be helpful in probing the di-Higgs production and the Higgs self-coupling further. With this motivation, we will study the prospects for probing nonresonant Higgs pair production at the HL-LHC and FCC-hh, with one of the Higgs bosons decaying exotically via $h \to aa \to 4\tau$ [Eq. (1.1)] and the other decaying via $h \to b\bar{b}$, thus, culminating in the $gg \to hh \to (h \to b\bar{b})(h \to aa \to 4\tau)$ final state.

It is worth reiterating here that one generically expects to first observe such exotic decays in single Higgs production channels and only later in hh production, owing to the lower rates of the latter. At $\sqrt{s} = 13$ TeV LHC, the hh production cross section in the ggF mode is $\sigma_{hh}^{ggF} = 31.05^{+2.2\%}_{-5.0\%}$ fb [39–46] at next-to-next-to-leading order (NNLO), which is roughly three orders of magnitude smaller than ggF induced single Higgs production. σ_{hh}^{ggF} improves only to $36.69^{+2.1\%}_{-4.9\%}$ fb and $1224^{+0.9\%}_{-3.2\%}$ fb [39–46] at $\sqrt{s} = 14$ and 100 TeV, respectively. Besides ggF, hh production at the LHC can also proceed via VBF, associated production with a vector boson (Vhh, $V = W^{\pm}/Z$), and associated production with a top-antitop pair ($t\bar{t}hh$). However, the latter processes have comparatively smaller cross sections, making them more challenging to probe. Despite the lower expected production rates in the di-Higgs channel, the possibility of exploiting novel final states, such as $gg \to hh \to (h \to b\bar{b})(h \to aa \to 4\tau)$, to probe the Higgs self coupling and scalar potential warrants further investigation.

It must be noted that both ATLAS and CMS collaborations have explored nonresonant Higgs pair production in numerous final states with a significant focus on the scenario where the Higgs boson decays via SM modes viz. $4b$ [47], $b\bar{b}\tau^+\tau^-$ [48,49], $b\bar{b}\gamma\gamma$ [50,51], $b\bar{b}WW^*$ [52], $WW^*\gamma\gamma$ [53], and $4W$ [54]. However, due to the nonobservation of any substantial excess over the SM expectation in these channels, upper limits have been derived on the di-Higgs production cross section (σ_{hh}) times SM branching ratio. In principle, BSM physics can impact the Higgs pair production cross section. Reference [55] discusses benchmark BSM scenarios like the Higgs Singlet model and the 2HDM model containing a heavy Higgs boson that can enhance the di-Higgs production rate. Moreover, deviations in the Higgs self-coupling can modify the hh production cross section. Reference [56] studies the custodial weak quadruplet extension and the Gegenbauer's twin model in detail that predict large Higgs self-coupling deviations. The current measurements from CMS in the combined $b\bar{b}ZZ$, *multilepton*, $b\bar{b}\gamma\gamma$, $b\bar{b}\tau\tau$, and $b\bar{b}b\bar{b}$ channels [57] and ATLAS in the combined $b\bar{b}\gamma\gamma$, $b\bar{b}\tau\tau$, and $b\bar{b}b\bar{b}$ channels [58] have constrained the di-Higgs signal strength (μ_{hh}) within $\mu_{hh} < 3.4$ and 2.4 at 95% CL, respectively. Discovery prospects for nonresonant di-Higgs production and its potential sensitivity to probe λ_h at the future hadron colliders have also been widely studied in the literature (see Refs. [59–81] and references therein), and they do not exhibit much promise at the HL-LHC. As discussed previously, the major bottleneck in nonresonant di-Higgs searches at the LHC is the low production rates, rendering them weaker than the single Higgs production channels, despite bearing a richer phenomenology. However, the rate bottleneck can be alleviated in various new physics scenarios. New physics models with extended Higgs sectors, modified top quark Yukawa interaction, or heavy color-charged states as in supersymmetric or extra-dimension theories, are a few typical examples [82–144]. In new physics scenarios with an extended Higgs sector, a heavier Higgs boson H which decays to two SM-like Higgs bosons $H \to hh$ can be resonantly produced ($gg \to H \to hh$), which can potentially increase the di-Higgs production rate. Studies on the future collider prospects of resonant di-Higgs production, with both SM-like Higgs bosons decaying via SM decay channels, can be found in Refs. [123,131,140,145–152]. In light of the possible presence of the exotic decay mode of the SM-like Higgs boson $h \to aa \to 4\tau$, the projected sensitivity for resonant di-Higgs searches warrants a thorough evaluation. Accordingly, we perform a detailed collider study to evaluate the projected reach of resonant di-Higgs production at the HL-LHC, in the $gg \to H \to hh \to (h \to b\bar{b})(h \to aa \to 4\tau)$ channel, for various combinations of heavy and light Higgs masses, m_H and m_a, respectively.

Another channel of interest is Higgs-Strahlung production $pp \to Zh$, a background in di-Higgs searches. The Zh production mode can also lead to the $2b4\tau$ final state with $Z \to b\bar{b}$ and h decaying via the exotic mode $h \to aa \to 4\tau$, thus, providing a supplementary channel in the search for exotic Higgs decays. The backgrounds of this channel include the $2b4\tau$ final state arising from nonresonant di-Higgs mode. In this work, we analyze the potential sensitivity for probing exotic Higgs decays in the $pp \to Zh \to (Z \to b\bar{b})(h \to aa \to 4\tau)$ channel at the HL-LHC and contrast the results with that from nonresonant di-Higgs searches.

The plan of the paper is as follows. In Sec. II, we study the projected reach for single Higgs production at the HL-LHC, with the Higgs boson decaying exotically $h \to aa \to 4\tau$. Both ggF (Sec. II A) and VBF (Sec. II B) production modes are considered, and our results are presented as projected upper limits on the Higgs boson signal strength $\mu_h^{ggF(VBF)} = \sigma_h^{ggF(VBF)}/\sigma_{h_{\rm SM}}^{ggF(VBF)}$ as a function of $\mathrm{Br}(h \to aa \to 4\tau)$ at 95% CL. Section III delves into the general kinematic features of the nonresonant di-Higgs production in the ggF channel, $gg \to hh \to b\bar{b}4\tau$, and explores its prospects at the HL-LHC and FCC-hh.

We further discuss the possibility of probing exotic Higgs boson decay in the Higgs-strahlung channel $pp \to Z(\to b\bar{b})h(\to aa \to 4\tau)$ in Sec. IV. The case of resonant di-Higgs production in the $gg \to H \to hh \to (h \to b\bar{b}) \times (h \to aa \to 4\tau)$ channel is studied in Sec. V. Finally, we summarize in Sec. VI.

II. THE $h \to 4\tau$ CHANNEL

The ggF channel is the dominant mode for single Higgs production at the LHC, with a cross section of $49.68^{+8.2\%}_{-8.7\%}$ pb at NNLO + NNLL (next-to-next-to-leading-logarithm) QCD and NLO electroweak(EW) [153] at $\sqrt{s} = 14$ TeV. The VBF production mode is the second largest, with a cross section of $4.260^{+2.2\%}_{-2.1\%}$ pb at NNLO QCD and NLO EW [153]. The ATLAS and CMS collaborations probed these production modes in various final states, viz. $h \to b\bar{b}$ [154,155], $\gamma\gamma$ [156,157], $\tau\tau$ [158], ZZ^* [157,159], WW^* [160,161], and $\mu\mu$ [162]. As discussed previously, current Higgs measurements at the LHC still have enough uncertainties to allow exotic decays of the SM-like Higgs boson, and such exotic Higgs decays are expected to appear in single Higgs search channels sooner than in nonresonant Higgs pair production channels due to larger rates. Correspondingly, the experimental collaborations have analyzed exotic decays of the Higgs boson $pp \to h \to aa$ at the current LHC in several final states, as discussed in Sec. I. Extending this search to HL-LHC is pertinent, which is precisely this section's goal. We study the projected reach for single Higgs production in ggF and VBF modes, with the Higgs decaying via $h \to aa \to 4\tau$, at the HL-LHC. The ggF channel is viable due to its large cross section, while the VBF channel offers a unique final state topology. On the other hand, the choice for the decay channel $h \to aa \to 4\tau$ is motivated by these three factors: (i) a modest signal production rate at the future LHC along with tractable background rates, (ii) a rich phenomenology offered by the multiple τs which could decay either leptonically (τ_l) or hadronically (τ_h) leading to a wide array of potential final states, and (iii) the absence of dedicated studies on this particular channel in the literature. We perform the analysis for several benchmark scalar masses, $m_a = 20$, 30, 40, 50, and 60 GeV, and combine both leptonic and hadronic decay modes of the τ lepton.

A. ggF production: $gg \to h \to aa \to 4\tau$

The kinematic features of the τ leptons in the process $gg \to h \to aa \to 4\tau$ have substantial dependence on the mass of the exotic scalar a. For illustrative purposes, we present the distributions for transverse momentum p_T of the four τ leptons at the truth level in Fig. 1. The τ leptons are p_T ordered as τ_i [$i = 1$–4], 1 being the hardest. For smaller values of m_a, viz. $m_a = 20$ GeV, the exotic scalars a are considerably boosted, which eventually translates to and largely regulates the boost associated with the τ leptons. This leads to a wide variation between the distributions for p_{T,τ_1} and p_{T,τ_4}. On the other hand, in the $m_a = 60$ GeV scenario, the as are produced almost at rest in the c.m. frame of h. In this case, the boost associated with the τ leptons is largely governed by the mass difference $m_a - m_\tau$. Hence, the p_{T,τ_1} and p_{T,τ_4} distributions for exotic scalars with larger mass manifest relatively close to each other. Implications from the dependence of $p_{T,\tau_i}(i = 1$–$4)$ distributions on m_a would become evident in the estimation of projected limits in the latter part of this section.

The main source of backgrounds are the inclusive 4ℓ and $h \to ZZ^* \to 4\ell$ ($\ell = e, \mu, \tau$) processes. Subdominant contributions arise from QCD-QED $4\ell 2\nu$, $4\ell 2b$, $t\bar{t}Z$, $t\bar{t}h$, $t\bar{t}ZZ$ and $t\bar{t}WW$. Signal and background events have been generated at LO with MadGraph5_aMC@NLO[1] [163] at $\sqrt{s} = 14$ TeV. Showering and hadronization effects in the signal and $h \to ZZ^* \to 4\ell$ background have been simulated with PYTHIA6 [164] along with CTEQ6L1 Parton distribution functions (PDF) set. We use PYTHIA8 [165] with the NN23LO PDF set for the rest of the backgrounds. Jets have been reconstructed using the anti-kT [166] algorithm with jet reconstruction parameters $R = 0.4$, and transverse momentum $p_T > 20$ GeV within the FastJet [167] framework. Detector response has been simulated with DELPHES-3.4.1 [168] using the detector card for ATLAS with the following modifications: b-tagging efficiency, as well as the efficiency of a light jet or c jet being mistagged as a b-tagged jet, are defined as functions of the jet p_T considering the medium working point (see Fig. 17 in Ref. [169]. For example, the b-tagging efficiency is about 62% for $p_T \sim 20$ GeV, while the c (light) jet mistagging efficiency is 12% (2%). Considering $p_T \sim 50$ GeV, the b-tag efficiency and c, light jet mistag efficiency is about 67% and 12%, 0.8%, respectively. τ-tagging efficiencies for the 1-prong and 3-prong τ-tagged jet (τ_h) are fixed at 55% and 50%, respectively, and $j \to \tau_h$ fake rate is set to 0.35% (see Fig. 3 in [170]).

The presence of exotic decay channels also modifies the total decay width of h (Γ_h) with respect to its SM value. In the present scenario, the modified total decay width of h is given by $\Gamma_h = \Gamma_{h_{\rm SM}} + \Gamma_{h\to aa\to 4\tau}$. Correspondingly, the SM branching ratios of h are scaled by the factor, $\sim(1 - {\rm Br}(h \to aa \to 4\tau))$.

Events with exactly four τ objects and zero b-tagged jets are selected. We consider both leptonic and hadronic decay modes of the τs and include these τ decay scenarios in the present analysis: (a) four τ-tagged jets ($4\tau_h$), (b) three τ_h and one ℓ ($\ell = e^\pm, \mu^\pm$), (c) two τ_h and two ℓ, and (d) one τ_h and three ℓ.[2] We want to mention that fake backgrounds

[1]The generation level cuts are tabulated in Appendix A (see Table XVIII).

[2]Unless otherwise specified, τ_h and ℓ will be collectively referred to as τ in the rest of the analysis. Here, we do not include the four ℓ final states as the $t\bar{t} + X$ backgrounds become very large with minor improvement in signal efficiency.

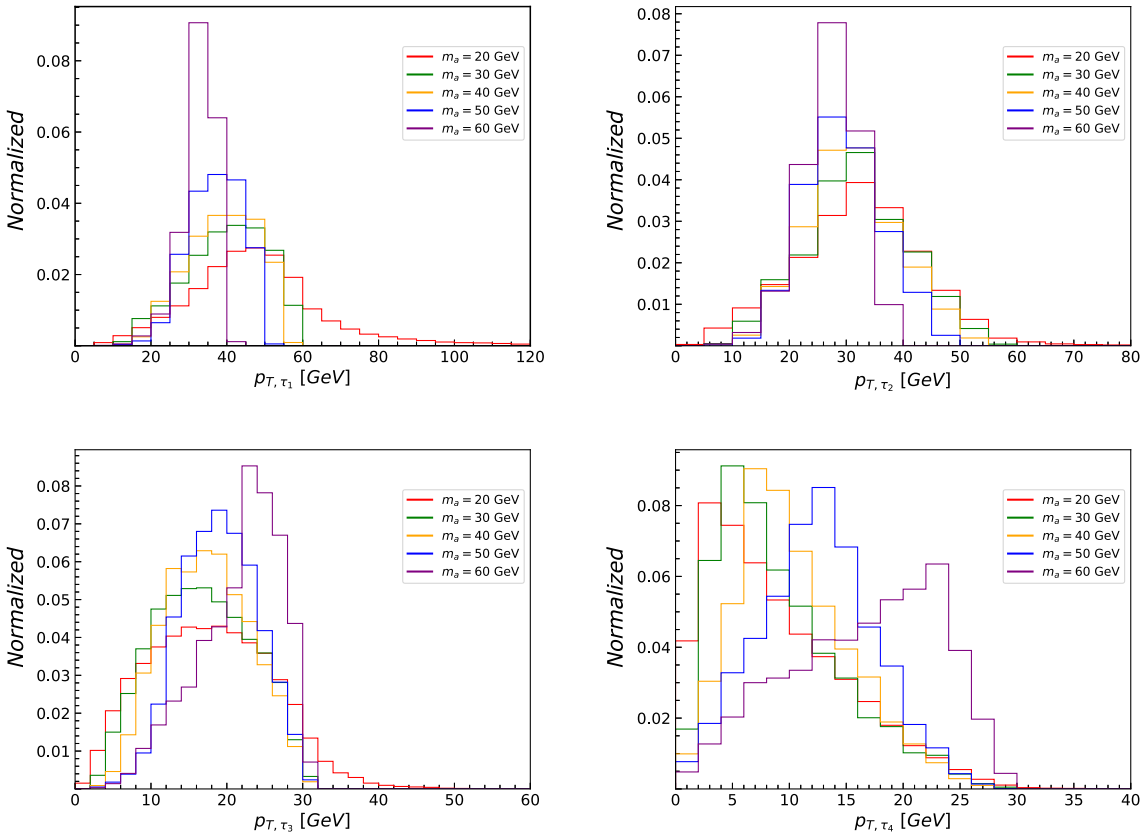

FIG. 1. Distributions for the transverse momentum p_T of the τ leptons at the truth level in the ggF induced single Higgs production channel $gg \to (h \to aa \to 4\tau)$, at $\sqrt{s} = 14$ TeV LHC.

can arise from a light jet faked as a hadronic τ. However, their contribution is suppressed because the mistagging efficiency is very low, and we demand four τ objects in the final state. We do not include these backgrounds in our analysis. The τ_h and ℓ must satisfy $p_T > 20$ GeV and >10 GeV, respectively. The minimum distance in the $\eta - \phi$ plane between the τ objects is as follows, $\Delta R(\tau_h, \tau_h) > 0.4$, $\Delta R(\tau_h, \ell) > 0.4$, and $\Delta R(\ell, \ell) > 0.1$.[3] The τ objects must be within $|\eta| < 3.0$. The veto on b jets is applied to reduce backgrounds like QCD-QED $4l2b$, $t\bar{t}Z$, $t\bar{t}h$, $t\bar{t}ZZ$, and $t\bar{t}WW$. Furthermore, events are required to satisfy the generation level cuts described in Table XVIII.

Several kinematic observables are reconstructed in order to discriminate the signal from the background through a multivariate analysis,

$$\Delta R_{\tau_i\tau_j}(i, j = 1-4; i \neq j), \quad \Delta R_{\tau\tau}^{\min}, \quad \Delta R_{\tau\tau}^{\max}, \quad p_{T,4\tau}, \quad m_{4\tau}^{\text{vis}}, \quad m_{T,h}, \quad \not{E}_T, \tag{2.1}$$

where $\Delta R_{\tau\tau}^{\min(\max)}$ represents the minimum (maximum) separation between any pair of τ objects, $p_{T,4\tau}$ and $m_{4\tau}^{\text{vis}}$ are the visible transverse momentum and invariant mass of the Higgs boson h, respectively, $m_{T,h}$ is the transverse mass of h, defined as $m_{T,h}^2 = (\sum_i E_{T,i})^2 - (\sum_i \vec{p}_{T,i})^2$ where i runs over the visible τ decay products and $\not{E}_T$, the missing transverse momentum. The training observables considered in Eq. (2.1) are chosen due to their sensitivity to the mass of the exotic scalar, which dictates the final state kinematics. The multivariate analysis is performed using the extreme gradient boosted, or XGBoost [171], technique, which is a decision tree-based machine learning algorithm. The multiclass classification algorithm is adopted through the MULTI:SOFTPROB objective function and three network hyperparameters are optimized, MAX DEPTH, η and λ. Here, MAX DEPTH is the maximum depth of a tree that XGBoost constructs, η is the learning rate, and λ is the L2 regularization applied to weights. Furthermore, the signal and background events in the training dataset are weighted according to their relative cross sections. The output from the trained network is a set of probability scores corresponding to each class. In other words, the model predicts, for every event, the probability of the event belonging to the signal and the different background classes.

[3]We choose the separation in the $\eta - \phi$ plane between two leptons to be >0.1 because the leptons coming from boosted τs are highly collimated and demanding a greater ΔR separation decreases the signal efficiency.

We rank the kinematic variables using SHAP (Shapley additive explanations) [172,173] based on how well they performed in the XGBoost analysis. SHAP is an individualized feature attribution method that uses the concept of Shapley values [174] to determine how much each feature contributed to the model's output. SHAP has emerged as a popular tool for interpreting machine learning results in collider studies [175–179]. The classification result for each event is equal to the total SHAP values of all the features in that specific event. We obtain a mean of the events' absolute SHAP values by averaging over all of the events. The influence of a variable in categorizing an event as a signal or one of the backgrounds increases with the SHAP value. The mean SHAP values of all the kinematic variables for exotic scalar of mass 20 (left) and 60 GeV (right), along with backgrounds, are summarized in Fig. 2. The variables, in this case, are ranked according to their feature importance. Signals and backgrounds are labeled with a class in multiclass classification. The different colors next to each feature on the y axis correspond to a class of signal or one of the backgrounds. The length of each colored bar for a given feature shows the contribution of that feature to classifying events into that class. It should be noted that $\Delta R_{\tau\tau}^{\min}$ has a more significant impact on the signal class for the 20 GeV scalar than it does for the 60 GeV case. This is because when the scalars have a mass of 20 GeV, the enhanced boost causes the τ objects to become collimated, reducing the minimum ΔR between τs and distinguishing the signal more from all other backgrounds. As the mass increases, the τs become more dispersed, and the signal loses the advantage of having a low $R_{\tau\tau}^{\min}$ in comparison to the backgrounds.

The training observables with the highest feature importance scores are $m_{T,h}$, $m_{4\tau}^{\rm vis}$, $\not{E}_T$, and $p_{T,4\tau}$. In Fig. 3, we show the distributions of these observables at the detector level for signal benchmarks corresponding to $m_a = 20$, 40, 60 GeV, and the relevant backgrounds. The signal efficiency and background yields B at the HL-LHC from the XGBoost analysis are shown in Table II. We also compute the signal yields S and signal significance at the HL-LHC, assuming $\mathrm{Br}(h \to aa \to 4\tau) = 0.1\%$. Here, signal significance is defined as $\mathcal{S} = S/\sqrt{S+B}$. The signal efficiency is almost similar for $m_a = 20$, 30, and 40 GeV. In Fig. 1, we observe that the distributions for p_{T,τ_4} for smaller m_a at the truth level peaks at $p_T \lesssim 10$ GeV. However, we apply stronger selection cuts on the visible decay products of these τ leptons at the detector level, $p_{T,\ell} > 10$ GeV and $p_{T,\tau_h} > 20$ GeV, which selects events only from the tail of the p_{T,τ_4} distributions in the $m_a = 20$, 30, and 40 GeV scenario, thereby, leading to lower signal efficiencies. On the other hand, the background yield increases with m_a. Overall, the significance falls from 6.0 at $m_a = 20$ GeV to 5.2 at $m_a = 40$ GeV. For higher values of m_a *viz* $m_a = 50$ and 60 GeV, the signal efficiency registers an improvement, leading to higher signal significance. The dominant contributions to the background yield arise from the 4ℓ and $h \to ZZ^* \to 4\ell$ ($\ell = e,\ \mu,\ \tau$) processes, as discussed previously. For example, in the $m_a = 60$ GeV scenario, the total background yield is 237, out of which 54% are inclusive 4ℓ events, 44% are $h \to ZZ^* \to 4\ell$ events and the other subdominant backgrounds comprise the remaining 2%. In Table II, we also show the signal significance given a systematic uncertainty of $\sigma_{\rm unc} = 5\%$, using $\mathcal{S} = S/\sqrt{S+B+((S+B)\times\sigma_{\rm unc})^2}$. Including systematic uncertainties barely reduces the significance due to relatively large $S/B \sim \mathcal{O}(1)$. It lowers only by 3–10% for $\sigma_{\rm unc} = 5\%$.

For comparison, we use two more models as multivariate methods. First, we perform a multivariate analysis using the boosted decision tree decorrelated (BDTD) algorithm in the TMVA framework. We optimize the following parameters while training the signal and background events, viz. number and length of decision trees, `NTrees` and

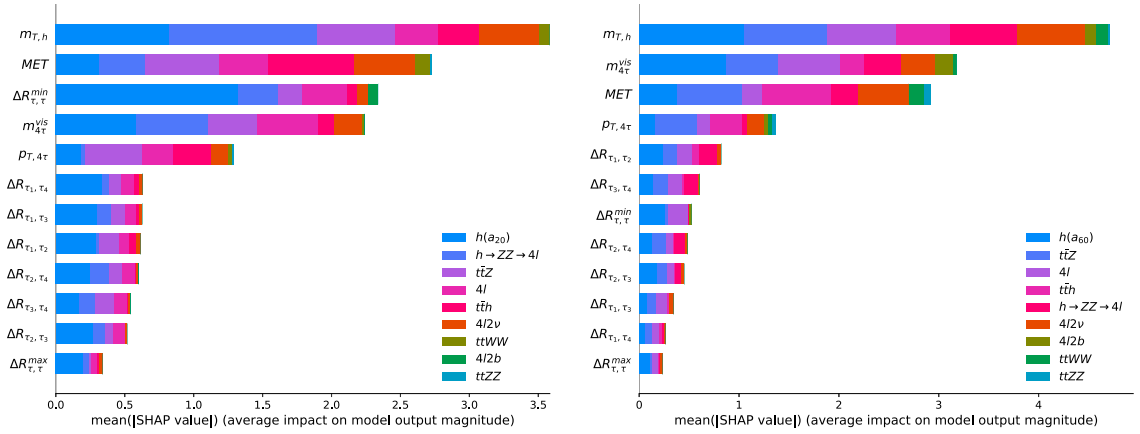

FIG. 2. Mean of the absolute SHAP values for the kinematic variables used to perform the XGBoost analysis for $m_a = 20$ (left) and 60 GeV (right) in the $gg \to h \to aa \to 4\tau$ channel, at $\sqrt{s} = 14$ TeV LHC with $\mathcal{L} = 3$ ab^{-1}. A higher absolute SHAP value indicates a higher rank.

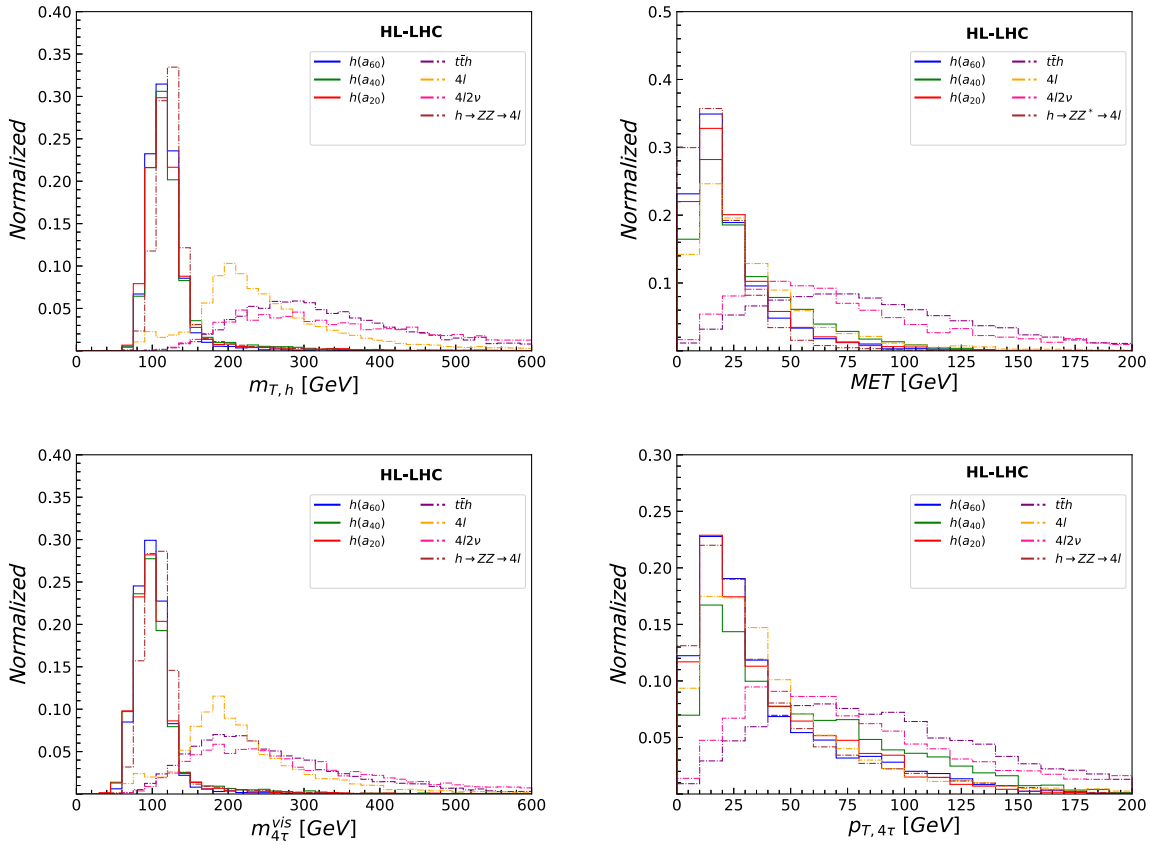

FIG. 3. Distributions for the transverse mass of the reconstructed Higgs boson $m_{T,h}$, missing transverse momentum $\not{E}_T$, invariant mass and transverse momentum for the visible 4τ system, $m_{4\tau}^{\rm vis}$ and $p_{T,4\tau}$, respectively, for signal benchmarks corresponding to $m_a = 20, 40, 60$ GeV, and relevant backgrounds, in the $gg \to h \to aa \to 4\tau$ channel at $\sqrt{s} = 14$ TeV LHC with $\mathcal{L} = 3$ ab^{-1}.

`MaxDepth`, respectively; minimum number of events (in %) in each leaf, `MinNodeSize` and `NCuts`. We utilize `Adaptive Boost` for boosting the weak classifiers. We maintain a stable Kolmogorov-Smirnov test score of >0.1 to avoid overtraining signal and background samples. The signal, background yields, and signal significance after the BDTD analysis are tabulated in Table III. The signal efficiency is poor compared to XGBoost results. For a scalar of mass, $m_a = 20$ (60) GeV, the XGBoost yields a signal significance of 6.0 standard deviations (s.d.) (10.3 s.d.). In contrast, BDTD results in 3.6 s.d. (2.9 s.d.), a decrease by 40(70)%.

Next, we use a deep neural network (DNN) model. The network consists of one input layer, three hidden layers with 16, 32, and 16 nodes, respectively, and one output layer with nine nodes for one signal and eight backgrounds.

TABLE II. Signal efficiency and background yields in the $gg \to h \to aa \to 4\tau$ channel at the HL-LHC from the XGBoost analysis. Signal yields and signal significance at the HL-LHC are also shown, under the assumption $\mathrm{Br}(h \to aa \to 4\tau) = 0.1\%$. Signal significance for 5% systematic uncertainty are shown in parenthesis.

$\sqrt{s}$ (TeV)	m_a (GeV)	Total background yield, B	Signal efficiency ($\times 10^{-4}$)	Signal yield, S	Significance (5% sys.)
14	20	50	4.3	64	6.0 (5.8)
	30	65	4.1	61	5.4 (5.2)
	40	87	4.2	63	5.2 (4.9)
	50	137	6	87	5.8 (5.3)
	60	237	15	221	10.3 (9.0)

TABLE III. Signal efficiency and background yields in the $gg \to h \to aa \to 4\tau$ channel at the HL-LHC from the BDTD-TMVA analysis. Signal yields and signal significance at the HL-LHC are also shown, under the assumption $\mathrm{Br}(h \to aa \to 4\tau) = 0.1\%$. Signal significance for 5% systematic uncertainty are shown in parenthesis.

$\sqrt{s}$ (TeV)	m_a (GeV)	Total background yield, B	Signal efficiency ($\times 10^{-4}$)	Signal yield, S	Significance (5% sys.)
14	20	58	2.4	35	3.6 (3.5)
	30	95	1.8	27	2.5 (2.2)
	40	105	2.4	36	3.0 (2.8)
	50	137	2.3	34	2.6 (2.3)
	60	48	1.7	25	2.9 (2.8)

TABLE IV. Signal efficiency and background yields in the $gg \to h \to aa \to 4\tau$ channel at the HL-LHC from the DNN analysis. Signal yields and signal significance at the HL-LHC are also shown, under the assumption $\mathrm{Br}(h \to aa \to 4\tau) = 0.1\%$. Signal significance for 5% systematic uncertainty are shown in parenthesis.

$\sqrt{s}$ (TeV)	m_a (GeV)	Total background yield, B	Signal efficiency ($\times 10^{-4}$)	Signal yield, S	Significance (5% sys.)
14	20	56	4.5	66	6.0 (5.8)
	30	66	4.4	66	5.7 (5.5)
	40	80	4.4	67	5.4 (5.1)
	50	150	6.4	96	6.1 (5.5)
	60	210	15	228	10.9 (9.8)

Each layer except the output layer uses the ReLu activation function. The final layer uses the Softmax function to output probabilities to each class label. The model minimizes categorical cross-entropy loss with a learning rate of 0.1, and the Adam optimizer. The model stops learning when the performance does not improve after five epochs to avoid overfitting.

Using the DNN, the results are listed in Table IV. There is a 5–6% improvement in performance using DNN. Since XGBoost and DNN have similar classification performances, we continue using XGBoost as our model for the rest of the analysis.

The measured Higgs signal strength, denoted as $\mu_h^{ggF} \equiv \sigma_h^{ggF}/\sigma_{h_{\mathrm{SM}}}^{ggF}$, is consistent with the SM predictions [57,180]. The observed σ_h^{ggF} is constrained within ~20% of $\sigma_{h_{\mathrm{SM}}}^{ggF}$, at 2 s.d. uncertainty.[4] In Fig. 4, we present the upper limit projections for $\mathrm{Br}(h \to aa \to 4\tau)$ as a function of m_a for the SM scenario $\sigma_h^{ggF} = \sigma_{h_{\mathrm{SM}}}^{ggF}$, or $\mu_h^{ggF} = 1$. We observe that the HL-LHC would be able to probe exotic Higgs decays up to $\mathrm{Br}(h \to aa \to 4\tau) \sim 0.025\%$ (0.015%) for $m_a = 20\,(60)$ GeV assuming SM production rates for h. With a 5% systematic uncertainty, the upper limits on $\mathrm{Br}(h \to aa \to 4\tau)$ become ~0.027% (0.018%) for $m_a = 20\,(60)$ GeV. The blue band illustrates the variation in the upper limit within a 2 s.d. interval of the current signal strength measurements obtained by the CMS [57] and ATLAS [180] collaborations.

As mentioned earlier, our present analysis does not consider backgrounds where a light jet might fake as a τ_h. Reference [32] analyzed the SS $\mu^{\pm}\mu^{\pm}+$ SS τ jets channel considering the dominant background from the fake $j \to \tau_h$ events while using a medium working point for τ identification. It must be noted that in prior studies (for example, see Fig. 9 in [181]), the medium working point

[4]The errors on the signal strength measurement by CMS and ATLAS have been combined in quadrature to obtain the approximate error on μ_h^{ggF}.

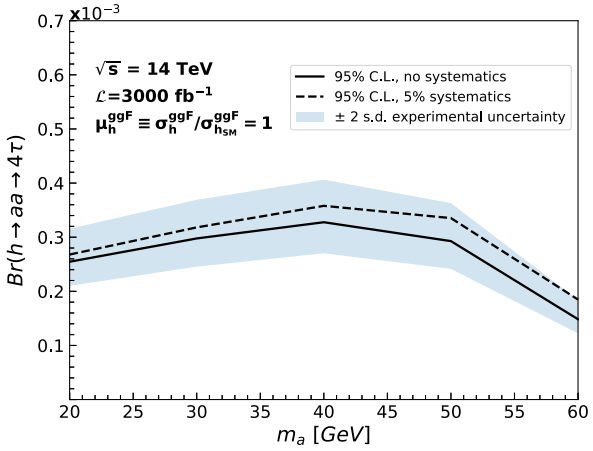

FIG. 4. Upper limit projection for $\mathrm{Br}(h \to aa \to 4\tau)$ at 95% CL, as a function of exotic scalar mass when μ_h^{ggF} is unity at $\sqrt{s} = 14$ TeV. The blue band represents the variation in $\mathrm{Br}(h \to aa \to 4\tau)$ within 2 s.d. interval of μ_h^{ggF} as measured by CMS [57] and ATLAS [180] collaborations. The solid and dashed lines refer to adding zero and 5% systematic uncertainty, respectively.

with one-prong τ-tagging efficiency of 55% corresponds to 1% $j \to \tau_h$ fake rate. In our analysis, we use τ-tagging efficiency of an MVA-based tagger [170], with 0.35% $j \to \tau_h$ fake rate for 55% one-prong τ-tagging efficiency. With an improved machine learning based τ tagger [182], the fake rate is expected to further reduce in the future. However, the backgrounds from $j \to \tau_h$ fakes might still play an important role in contaminating our signal, which can be estimated by choosing a tighter working point for τ identification. For example, choosing a τ-tagging efficiency of 30% for $m_a = 60$ GeV and assuming that the total background yield doubles upon considering the contribution of additional backgrounds from $j \to \tau_h$ fakes, we obtain an upper limit on $\mathrm{Br}(h \to aa \to 4\tau) \sim 0.06\%$ (0.07%), assuming 0% (5%) systematic uncertainty. This limit is roughly four times weaker than the upper limit presented in Fig. 4.

Our current analysis methodology yields subpar signal efficiency for scalars with $m_a < 20$ GeV. In this scenario, the decay products of τs are collimated and hard to isolate. The requirement of four τ objects at the detector level becomes too strict to achieve decent signal efficiency. For instance, even with a large ggF production cross section at HL-LHC, we expect to observe only five events for $\mathcal{L} = 3$ ab^{-1}, for an exotic scalar of mass $m_a = 10$ GeV, leading to a signal significance of only 1.33. The upper limit on the branching ratio for the exotic Higgs decay considering the SM case is almost an order of magnitude weaker than the $m_a \geq 20$ GeV scenarios and comes about $\mathrm{Br}(h \to aa \to 4\tau) \sim 0.168\%$. Due to the weaker sensitivity, we do not consider very low-mass exotic scalars in the present analysis. However, it must be noted that the projection above for $m_a = 10$ GeV are stronger than the

current limits on $\mathrm{Br}(h \to aa \to 4\tau) \sim 3\%$ [26] by roughly an order of magnitude.

The analysis done in this paper utilizes no kinematic observables which depend on the exotic scalar mass, which is a free parameter. However, we have performed an alternate analysis by reconstructing the exotic scalars from the final state τs. The analysis depends on the choice of m_a, and we see that the results are comparable. At the detector level, the presence of multiple missing particles (ν) produced from τ decays makes it challenging to reconstruct a. To circumvent this issue, we adopt the collinear mass approximation (CMA) technique [183]. This technique is based on two assumptions: visible and invisible components from τ decays are nearly collinear ($\theta_{\mathrm{vis}} \sim \theta_\nu$ and $\phi_{\mathrm{vis}} \sim \phi_\nu$), and neutrinos are the only source of missing energy. In the present study, the validity of the first assumption is determined by the difference between m_a and m_τ, and the boost carried by m_a. Low mass exotic scalars, $m_a \sim 20$ GeV, are considerably boosted due to the large mass gap with m_h while heavier values of m_a ($\sim$60 GeV) are produced almost at rest in the rest frame of h. However, as discussed previously, the τ lepton is boosted in the latter case due to the relatively large mass gap between a and τ. These conditions validate the first approximation of the CMA technique. The second approximation naturally holds since the only missing energy source is the neutrinos produced from the τ decays. One drawback of this technique is its high sensitivity to $\not{E}_T$ resolution, leading to overestimating the reconstructed Higgs mass with long tails in the distribution.

Since the final state decay products of exotically decaying Higgs, τs, are identical at the detector level, the goal is to choose the right pair of τs to reconstruct the two exotic scalars. We first check this at the parton level where the full kinematics is known. The four visible τ decay objects can be grouped into two pairs corresponding to the two equal mass exotic scalars, a_1 and a_2, in three independent ways, with one of them being the correct τ pair. First, we choose the following variables to see their potential in having similar features across most of the events for the correct pairing, $\Delta R^1_{\tau\tau}$, $\Delta R^2_{\tau\tau}$, $m^{\mathrm{col}}_{4\tau}$, $(m^{a1_{\mathrm{col}}}_{\tau\tau}/m^{a2_{\mathrm{col}}}_{\tau\tau})$, $(m^{a1_{\mathrm{col}}}_{\tau\tau} - m^{a2_{\mathrm{col}}}_{\tau\tau})$, and χ^2_{min}. Here, $\Delta R^1_{\tau\tau}$ and $\Delta R^2_{\tau\tau}$ are ΔR separations between τs in a pair which are used to construct light scalars. The $m^{a1_{\mathrm{col}}/a2_{\mathrm{col}}}_{\tau\tau}$ and $m^{\mathrm{col}}_{4\tau}$ are the collinear mass of a_1/a_2 and exotically decaying 125 GeV Higgs boson, respectively, as defined in the previous paragraph. In case of χ^2_{min}, we choose the combination of τs that minimizes the function

$$\chi^2_{\mathrm{min}} = \left[\frac{((m^{a1_{\mathrm{col}}}_{\tau\tau})^2 - m_a^2)^2}{\sigma^4_{a1}} + \frac{((m^{a2_{\mathrm{col}}}_{\tau\tau})^2 - m_a^2)^2}{\sigma^4_{a2}}\right], \quad (2.2)$$

where $\sigma_{a1/a2} = 0.1 \times m^{a1_{\mathrm{col}}/a2_{\mathrm{col}}}_{\tau\tau}$ [184]. Among these six variables, over most events, the χ^2_{min} performs better with a minimum value for the correct τ pair. So, we choose the χ^2_{min} to reconstruct the exotic scalars in our analysis. However, this method has some additional complications:

(1) For a selected pair of τs, they must contain oppositely charged τs to reconstruct the neutral exotic scalars. This information is absent in the χ^2 minimization procedure. While this can be easily implemented for a leptonically decaying τ, there is an ambiguity in defining the charge of a hadronic τ or τ jet. We explicitly checked this in Delphes, and a significant number of events contain τ jets with charges other than ± 1. In those cases, assigning τ pairs to an exotic scalar and constructing variables using them might be misleading.

(2) We are using the mass of the exotic scalar while calculating χ^2_{min}. But we do not have that knowledge in actual experiments. Hence, we choose to continue with our methodology, which is not dependent on exotic scalar mass information.

In continuation of the CMA technique, we do not remove those events having different charges in a τ pair. Instead, we choose the τ pairs from the second χ^2 minimum. This helps in improving signal efficiency. The $\tau\tau$ pairing derived from Eq. (2.2) is also used to reconstruct the visible invariant mass of the exotic scalars, $m^{a1_{\mathrm{vis}}}_{\tau\tau}$ and $m^{a2_{\mathrm{vis}}}_{\tau\tau}$, and we include them in XGBoost analysis. After performing the analysis, we found no significant improvement in the final results using these mass-dependent variables. For scalars of mass $m_a = 20$ GeV, this methodology gives a signal significance of 6. As a result, we do not employ this method further in this study, but we acknowledge that it has room for improvement.

B. *VBF* production: $pp \to (h \to aa \to 4\tau)jj$

Having discussed the HL-LHC prospects for *ggF* induced single Higgs production channel, we now focus on single Higgs production in the *VBF* mode $pp \to hjj \to (h \to aa \to 4\tau)jj$. The dominant background stems from the QCD-QED $4\ell 2j$ process. Subdominant background contributions can arise from QCD-QED $4\ell 2b$, $t\bar{t}Z, t\bar{t}h, t\bar{t}ZZ$, and $t\bar{t}WW$ processes. We select events containing exactly four τ objects with at least one τ-tagged jet and at least two light jets in the final state. Figure 16 in Appendix B shows the $p_{T,\tau}$ distributions at the parton-level for the five signal benchmarks. The choice for τ objects is similar to that in Sec. II A. The trigger cuts for the final state objects are

$$p_{T,\tau_\ell} > 10\,\mathrm{GeV}, \quad p_{T,\tau_h} > 20\,\mathrm{GeV}, \quad p_{T,j_1/j_2} > 30\,\mathrm{GeV},$$
$$|\eta_{\tau_\ell/\tau_h}| < 3.0, \quad |\eta_{\tau_{j_1/j_2}}| < 4.0, \quad (2.3)$$

where j_1 and j_2 are the hardest-p_T light jets in the final state. The *VBF* Higgs production channel leads to a unique topology with the *VBF* jets produced back to back in the

forward regions of the detector. Prompted by the large pseudorapidity difference between the VBF jets and a large invariant mass, we require events to satisfy $\eta_{j_1}.\eta_{j_2} < 0$ and $m_{j_1 j_2} > 500$ GeV. Furthermore, the pseudorapidity difference between these VBF jets $\Delta\eta_{j_1 j_2}$ is used as a training observable in the XGBoost analysis. We also veto events containing any b-tagged jet with $p_T > 30$ GeV and $|\eta| < 3$ in order to suppress the $t\bar{t} + X$ backgrounds. Kinematic cuts that are specific to the VBF topology viz. $m_{j_1 j_2} > 500$ GeV is also imposed at the event generation level to improve the population of events in the phase space of our interest. Similar to Sec. II A, we also apply the ΔR cuts, $\Delta R_{\tau_h,\tau_{h/\ell}} > 0.4$, and $\Delta R_{\tau_\ell,\tau_\ell} > 0.1$. We also apply the generation level cuts, which are summarized in Appendix A, along with the signal and background cross sections.

We next turn our attention to the multivariate XGBoost analysis to discriminate the exotically decaying VBF Higgs signal from the SM backgrounds. The optimization is performed for the five signal benchmarks considered in Sec. II A. The following kinematic observables are used to perform the training,

$$\Delta R_{\tau_i\tau_j}(i,j = 1-4; i \neq j), \quad \Delta R^{\min}_{\tau\tau}, \quad \Delta R^{\max}_{\tau\tau}, \quad H_T, \quad m_{T,h}, \quad m^{\text{vis}}_{4\tau}, \quad p_{T,jj}, \quad m_{jj}, \quad \Delta\eta_{jj}, \quad \Delta R_{jj,4\tau}, \quad \not{E}_T. \tag{2.4}$$

Here, H_T is the scalar p_T sum of the visible τ objects and the hardest two VBF jets in the final state, $p_{T,j_1 j_2}$ is the transverse momentum for the pair of VBF tagged jets, $\Delta R_{jj,4\tau}$ is the ΔR between the VBF dijet system and the visible Higgs system reconstructed from the visible τs. The other kinematic observables in Eq. (2.4) have their usual meanings. The relative importance of the training observables in Eq. (2.4) in the XGBoost analysis is measured using SHAP analysis. We present the results for the $m_a = 20$ and 60 GeV scenarios in Fig. 5. The top four observables with highest SHAP scores for the $m_a = 60$ GeV scenario are $m^{\text{vis}}_{4\tau}$, $m_{T,h}$, H_T, and $\not{E}_T$.

For illustrative purposes, we show their distributions at the detector level in Fig. 6. We observe that $m^{\text{vis}}_{4\tau}$ and $m_{T,h}$ distributions for the signal benchmarks peak at $\lesssim m_h$ due to the decay products from Higgs resonance comprising of missing energy from the neutrinos. On the other hand, the background distributions peak at higher values and are relatively flatter, thereby leading to excellent signal-to-background discrimination. The H_T distributions for the signal benchmarks and background processes also exhibit a similar trend. In the distributions for $\not{E}_T$, the signal benchmarks lead to peaks at $\not{E}_T \sim 30$–40 GeV. Here, the missing energy arises mainly due to neutrinos from the decay of τ leptons. We observe that the $\not{E}_T$ distributions for the $4\ell 2b$ background process overlap considerably with the signal benchmark. However, the rest of the backgrounds are relatively flatter, with peaks at higher values.

The signal efficiency and background yields at the HL-LHC for the five signal benchmarks considered in Sec. II A are shown in Table V. Keeping in line with the discussion in Sec. II A, we also compute the signal yields and the signal significance under the assumption $\text{Br}(h \to aa \to 4\tau) = 0.1\%$. For a given signal benchmark, the significance from the VBF channel is lower than that from the ggF channel (cf. Table II) due to a smaller production rate for the former. Signal efficiency and background yields increase with m_a. However, the relative growth for signal efficiency is larger than the background yields leading to an overall improvement for the signal significance.

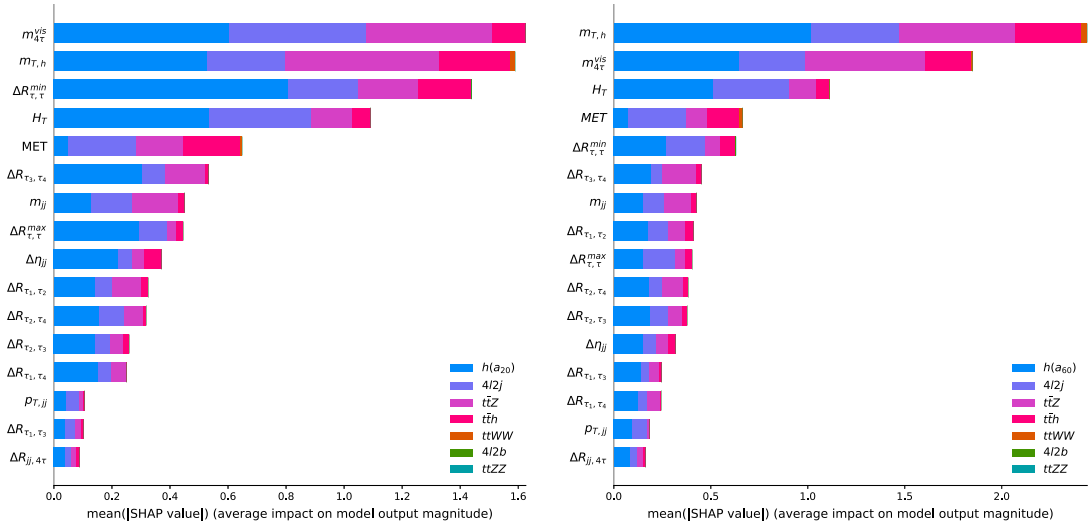

FIG. 5. Mean of absolute SHAP values for the kinematic observables [Eq. (2.4)] used to perform the XGBoost analysis for $m_a = 20$ (left) and 60 GeV (right) in the $VBF\ pp \to hjj \to (h \to aa \to 4\tau)jj$ channel, at the HL-LHC. A higher absolute SHAP value indicates a higher rank.

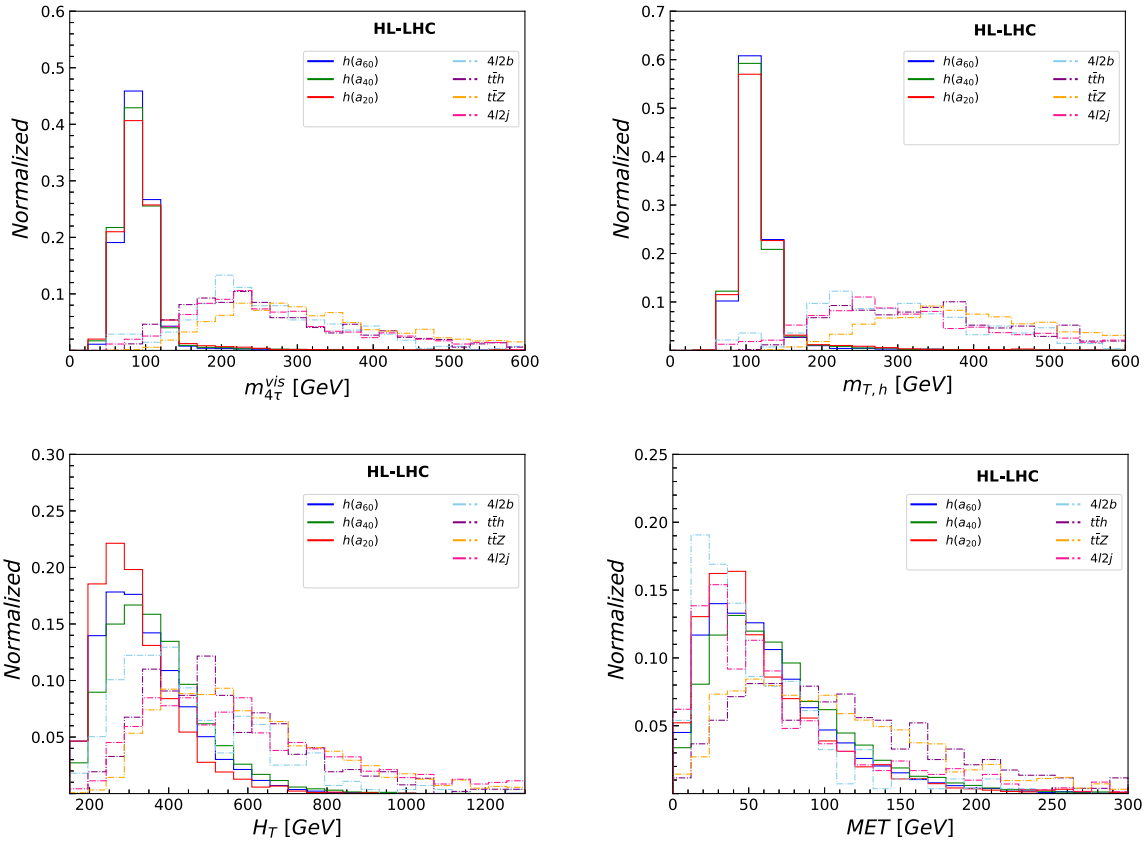

FIG. 6. Distributions for $m_{4\tau}^{\rm vis}$, $m_{T,h}$, H_T, and $\not{E}_T$ at the detector level for different signal benchmarks with exotic scalar masses $m_a = 20$, 40, and 60 GeV in the VBF single Higgs production channel $pp \to hjj \to (h \to aa \to 4\tau)jj$. Distributions for the QCD-QED $4\ell 2j$, $4\ell 2b$, $t\bar{t}Z$, and $t\bar{t}h$ background processes, are also shown. We consider $\sqrt{s} = 14$ TeV LHC with $\mathcal{L} = 3$ ab^{-1}.

In Table V, the significance values shown within parentheses correspond to a systematic uncertainty of 5%. We observe that the signal significance values remain almost unaffected by systematic uncertainties due to relatively large $S/B \sim \mathcal{O}(1)$ values. The results shown in Table V can be translated into upper limits in the plane of Br$(h \to aa \to 4\tau)$ as a function of m_a as shown in Fig. 7, under the assumption of $\mu_h^{VBF} = 1$, where $\mu_h^{VBF} = \sigma_h^{VBF}/\sigma_{h_{\rm SM}}^{VBF}$. For $m_a = 20$ GeV

TABLE V. The signal, background yields, and signal significance at the HL-LHC after the XGBoost analysis in the VBF single Higgs production where Higgs decays via $h \to aa \to 4\tau$. Here, we assume Br$(h \to aa \to 4\tau) \sim 0.1\%$.

$\sqrt{s}$ (TeV)	m_a (GeV)	Total background yield, B	Signal efficiency ($\times 10^{-4}$)	Signal yield, S	Significance (5% sys.)
14	20	5	3.8	5	1.5 (1.5)
	30	6	8.4	11	2.6 (2.6)
	40	7	10	13	2.9 (2.9)
	50	8	12	15	3.1 (3.1)
	60	9	15	20	3.7 (3.6)

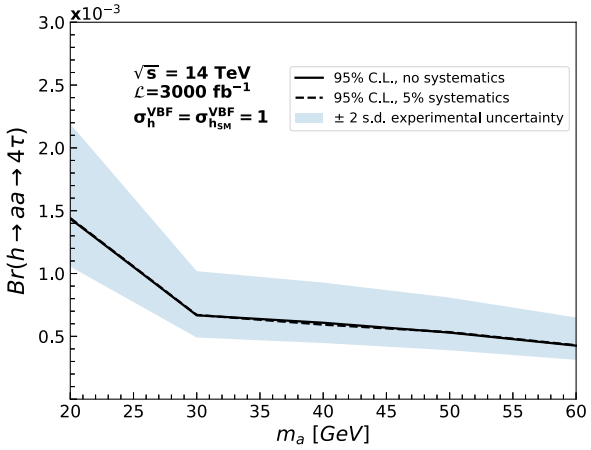

FIG. 7. Upper limit projection for Br$(h \to aa \to 4\tau)$ at 95% CL as a function of exotic scalar mass when μ_h^{VBF} is unity at $\sqrt{s} = 14$ TeV. The blue band represents the variation in Br$(h \to aa \to 4\tau)$ within 2 s.d. interval of μ_h^{VBF} as measured by CMS [57] and ATLAS [180] collaborations. The solid and dashed lines refer to adding zero and 5% systematic uncertainty, respectively.

(60 GeV), the HL-LHC would be able to probe exotic Higgs branching ratios as small as $\mathrm{Br}(h \to aa \to 4\tau) \lesssim 0.14\%$ (0.043%) through searches in the VBF Higgs production channel at 2 s.d. uncertainty. The observed σ_h^{VBF} at the LHC is constrained within ∼40% of $\sigma_{h_{\mathrm{SM}}}^{VBF}$ at 2 s.d. uncertainty [57,180]. The blue band displays the variation in the upper limit within 2 s.d. uncertainty of μ_h^{VBF} measurements.

As previously discussed in Sec. I, signatures for exotic Higgs decay are expected to be observed in single Higgs production channels before in nonresonant di-Higgs searches. Nonetheless, it must be noted that Higgs pair production offers a far richer phenomenology, which can be utilized to complement the potential sensitivity from single Higgs production channels. Therefore, in the following section, we perform a detailed collider study to estimate the future potential at the HL-LHC to probe exotic Higgs decays in the nonresonant di-Higgs production.

III. NONRESONANT HIGGS PAIR PRODUCTION: $gg \to hh \to (h \to b\bar{b})(h \to aa \to 4\tau)$

In this section, our focus is the nonresonant di-Higgs production channel with one Higgs boson decaying into $b\bar{b}$ and the other decaying into a pair of light exotic scalars: $gg \to hh \to (h \to b\bar{b})(h \to aa \to 4\tau)$, at $\sqrt{s} = 14$ TeV HL-LHC.

The major sources of background are $t\bar{t}h$, $t\bar{t}Z$, and $Zh \to (Z \to b\bar{b})(h \to aa \to 4\tau)$ processes. In addition, QCD-QED $4\ell 2b$, $t\bar{t}ZZ$, and $t\bar{t}WW$ contribute subdominantly. The signal and background events are generated using the simulation chain considered in Sec. II. The jet reconstruction parameters are fixed at $R = 0.4$ and $p_T > 20$ GeV. Other event reconstruction parameters remain unchanged from Sec. II.

We first perform a traditional cut-and-count collider analysis, optimizing the cuts on selected kinematics observables. Afterwards, we follow a machine-learning-based approach using the XGBoost algorithm. Here again, we consider five signal benchmarks corresponding to different exotic scalar masses $m_a = 20$, 30, 40, 50, and 60 GeV. Then, we translate our results into projected upper limits on $\mathrm{Br}(h \to aa \to 4\tau)$ with the condition that $\sigma_{hh}^{ggF} = \sigma_{hh,SM}^{ggF}$. Under this assumption, we also estimate the projected upper limits for the di-Higgs signal strength factor $\mu_{hh}^{ggF} = \sigma_{hh}^{ggF}/\sigma_{hh,SM}^{ggF}$ as a function of $\mathrm{Br}(h \to aa \to 4\tau)$ for different values of m_a.

We select events containing exactly two b-tagged jets with $p_T > 30$ GeV and $|\eta| < 3.0$, and four τ objects. Both leptonic and hadronic τ decay modes are considered. Similar to the analysis in Sec. II, the fully leptonic final state from exotic Higgs decay is ignored due to the small production rate and complex combinatorial ambiguity. The selected events are also required to pass the τ trigger cuts (see Sec. II A) and the generation level cuts, summarized in Table XIX. Furthermore, $p_{T,b_1} > 40$ GeV (b jets are p_T sorted), and $0.4 < \Delta R_{b_1 b_2} < 2$.

Having discussed the event selection cuts, we next turn our attention towards reconstructing the di-Higgs system. One of the Higgses is reconstructed upon requiring 90 GeV $< m_{bb} <$ 130 GeV following the optimization in Ref. [66]. In addition, we require $p_{T,b\bar{b}} > 80$ GeV. However, reconstructing the exotically decaying h is challenging due to the presence of multiple invisible particles in the final state from the decay of the τ leptons. Bypassing this complexity, we reconstruct the visible invariant mass of the exotically decaying h, $m_{4\tau}^{\mathrm{vis}}$, similar to single Higgs production. In Fig. 8, we illustrate the $m_{4\tau}^{\mathrm{vis}}$ distributions for the signal benchmarks and the dominant backgrounds at $\sqrt{s} = 14$ TeV. For both c.m. energies, we observe that the peak for $m_{4\tau}^{\mathrm{vis}}$ distributions for the signal process and the Zh background falls close to 80 GeV. On the other hand, the dominant $t\bar{t} + X$ backgrounds peak at a higher value and are flatter. Overall, $m_{4\tau}^{\mathrm{vis}}$ proves to be an excellent discriminator against the associated $t\bar{t}$ backgrounds.

Another category of observables of considerable interest is the angular correlations between the τs. In Fig. 8, we present the $\Delta R_{\tau\tau}^{\mathrm{min(max)}}$ distributions, which corresponds to the smallest (largest) ΔR separation between any pair of visible components from the decay of τ leptons. Both observables exhibit excellent discrimination against the $t\bar{t}h$ and $t\bar{t}Z$ backgrounds. We would like to point out the following observations:

(1) Two distinct peaks are observed in the $\Delta R_{\tau\tau}^{\mathrm{min}}$ distributions for the signal process, $0.1 < \Delta R_{\tau\tau}^{\mathrm{min}} < 0.4$ and $\Delta R_{\tau\tau}^{\mathrm{min}} > 0.4$. This segregation is an implication of the ΔR selection cuts. While the minimum distance between the visible components of two leptonically decaying τ leptons (τ_ℓ) is $\Delta R \gtrsim 0.1$, the minimum separation between τ_h pairs or $\{\tau_h, \tau_\ell\}$ pair must be greater than $\Delta R \gtrsim 0.4$. Hence the $\Delta R_{\tau\tau}^{\mathrm{min}} < 0.4$ region is associated which those events where the least separated τs are leptonic.

(2) The ΔR separation between the τ leptons produced from the decay of an exotic scalar $a \to \tau\tau$ is inversely correlated to the mass gap between h and a. As a result, the τ siblings with identical mother a would be more collimated in the $m_a =$ 20 GeV scenario compared to the $m_a = 60$ GeV scenario. Let us take the example of $m_a = 20$ GeV. Here, the light exotic Higgs boson is produced with a relatively larger boost owing to its small mass, leading to highly collimated decay products. This further implies a narrower peak for smaller m_a. As a result, the smallest ΔR separation is exhibited by the τ pairs produced from the same light scalar. On the other hand, at relatively higher m_a values, $m_a \gtrsim 30$ GeV, τ decay products from different light scalars start constituting $\Delta R_{\tau\tau}^{\mathrm{min}}$.

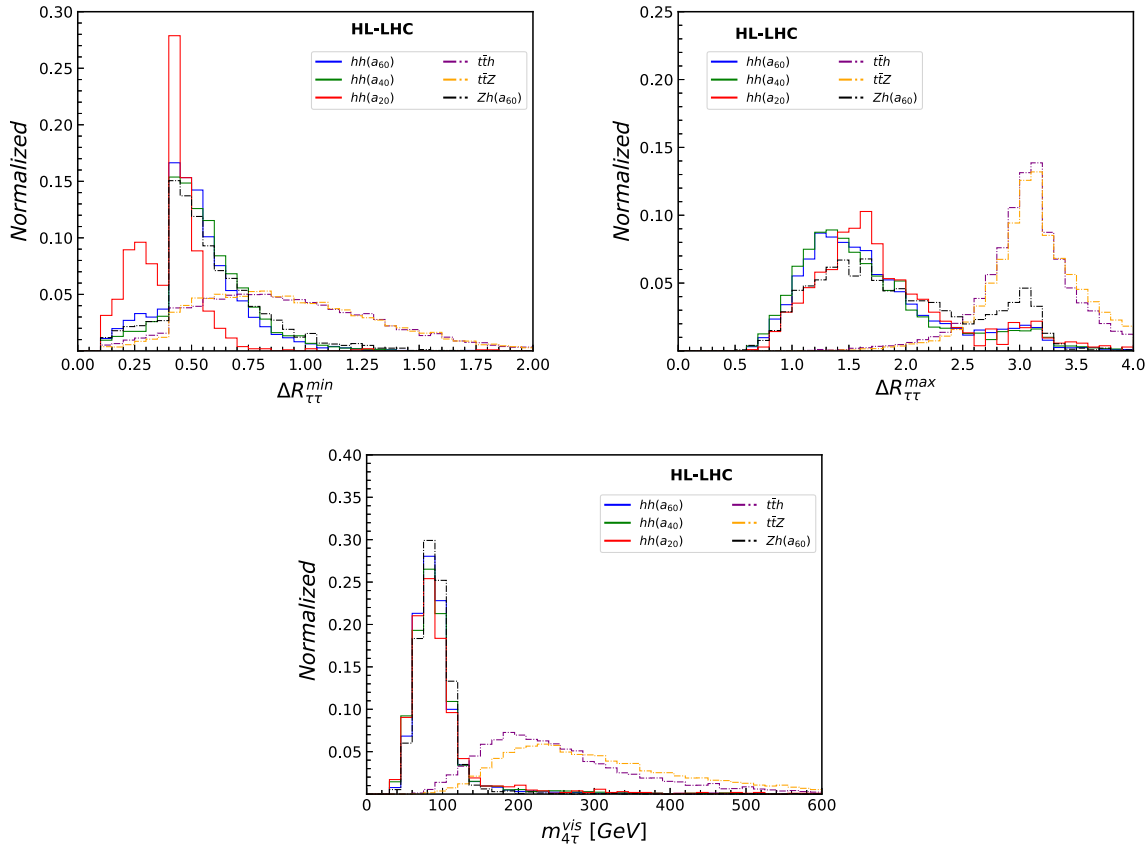

FIG. 8. Distributions of $\Delta R_{\tau\tau}^{\min}$, $\Delta R_{\tau\tau}^{\max}$, and $m_{4\tau}^{\rm vis}$ for signal benchmarks $m_a = 20, 40, 60$ GeV, and dominant backgrounds, in the $pp \to hh \to (h \to b\bar{b})(h \to aa \to 4\tau)$ channel at $\sqrt{s} = 14$ TeV LHC.

(3) The peak for the $\Delta R_{\tau\tau}^{\max}$ distributions exhibit a mild shift towards larger values with decreasing m_a. At smaller m_a, the τ siblings are highly collimated with their three momentum vectors roughly pointing in the same direction as their parent scalar a. Therefore, the τ pair candidates with the largest ΔR separation are more likely to arise from different scalar parents at smaller values of m_a.

Taking into account these observations, we perform a cut-based collider analysis by optimizing the selection cuts on $m_{4\tau}^{\rm vis}$, $\Delta R_{\tau\tau}^{\min}$, and $\Delta R_{\tau\tau}^{\max}$. We analyze five signal benchmarks considered in Sec. II at the HL-LHC and FCC-hh. Our goal is to maximize the signal significance $\mathcal{S} = S/\sqrt{S+B}$.

In Table VI, we summarize the basic selection cuts and the optimized cuts on $m_{4\tau}^{\rm vis}$, $\Delta R_{\tau\tau}^{\min}$, and $\Delta R_{\tau\tau}^{\max}$. We observe that the optimized cuts on $m_{4\tau}^{\rm vis}$ get slightly stronger with larger values of m_a. For example, for $m_a = 20$ GeV, the signal significance is maximized at $m_{4\tau}^{\rm vis} < 140$ GeV while at $m_a = 60$ GeV, the signal significance is maximized at $m_{4\tau}^{\rm vis} < 120$ GeV. We further observe that the optimized selection cuts get weaker with increasing m_a since the peak of $\Delta R_{\tau\tau}^{\min}$ distributions shift to lower values with decreasing

TABLE VI. Basic selection and optimized cuts imposed in the cut-and-count analysis for $pp \to hh \to (h \to b\bar{b})(h \to aa \to 4\tau)$ channel at HL-LHC.

Basic selection cuts
$p_{T,b_1(b_2)} > 40(30)$ GeV, $0.4 < \Delta R_{bb} < 2.0$
90 GeV $< m_{bb} <$ 130 GeV
$p_{T,bb} > 80$ GeV
Optimized cuts for 14 TeV analysis
$m_{4\tau}^{\rm vis} < [140, 130, 120, 120, 120]$ GeV for $m_a = [20, 30, 40, 50, 60]$ GeV
$\Delta R_{\tau\tau}^{\min} < [0.6, 0.9, 1.2, 1.2, 1.2]$ and $\Delta R_{\tau\tau}^{\max} < [2.4, 2.6, 2.6, 2.8, 2.8]$ for $m_a = [20, 30, 40, 50, 60]$ GeV

m_a. A similar variation is also exhibited by the optimized cuts on $\Delta R_{\tau\tau}^{\max}$.

The cut-flow information and the signal significance at the HL-LHC are presented in Tables VII. Adopting a conservative approach, we consider $\mathrm{Br}(h \to aa \to 4\tau) = 10\%$ [2,32] while computing the signal and Zh background yields. We find that significance increases with m_a. At the HL-LHC, we obtain a significance of ∼1.1 for $m_a = 20$ GeV, which increases to ∼2.0, 2.2, 2.3, and 2.5 at $m_a = 30, 40, 50$, and 60 GeV, respectively. In addition to the optimized cuts on $m_{4\tau}^{\mathrm{vis}}$, $\Delta R_{\tau\tau}^{\min}$, and $\Delta R_{\tau\tau}^{\max}$, the selection cuts on $p_{T,\tau}$ plays a pivotal role towards improving the significance with m_a. For $m_a \sim 20$ GeV, the τs from the $a \to \tau\tau$ decay is produced rather softly compared to a scenario where m_a is heavier. This behavior is illustrated in Fig. 17, Appendix B where we present the $p_{T,\tau}$ distributions at the parton-level for the five signal benchmarks at $\sqrt{s} = 14$ TeV. At the basic selection stage, we require $p_{T,\tau_h} > 20$ GeV and $p_{T,\tau_l} > 10$ GeV. The signal efficiency is the highest for $m_a = 60$ GeV and decreases with m_a. This hierarchy percolates down to the final stage of cut-based optimization. The signal efficiency for smaller values of m_a could be potentially improved through smaller and optimized trigger cuts on p_{T,τ_h} and $p_{T,\ell}$ at the HL-LHC. Such studies inspire a detailed analysis of the projected low-p_T trigger efficiency at future colliders and are beyond the scope of the present work.

TABLE VII. Signal and background yields in the $pp \to hh \to (h \to b\bar{b})(h \to aa \to 4\tau)$ channel, at each step of the cut-based analysis for the signal benchmarks $m_a = 20, 30, 40, 50$, and 60 GeV and the dominant backgrounds at the HL-LHC. Signal significance at the HL-LHC is also shown for $\mathrm{Br}(h \to aa \to 4\tau) = 10\%$.

	Event rates at $\sqrt{s} = 14$ TeV with $\mathcal{L} = 3$ ab^{-1}								
		Backgrounds							
Cut flow	Signal	$t\bar{t}h$	$t\bar{t}Z$	Zh	$4\ell 2b$	$t\bar{t}ZZ$	$t\bar{t}WW$	$\frac{S}{(S+B)}$	Significance
				$m_a = 20$ GeV					
$p_{T,b}$, ΔR_{bb}	2.8	34	81	2.3	2.0	0.72	1.4	0.023	0.25
m_{bb}	2.0	12	26	0.40	0.66	0.24	0.46	0.047	0.30
$p_{T,bb}$	1.9	11	25	0.38	0.63	0.23	0.44	0.048	0.30
$m_{4\tau}^{\mathrm{vis}}$	1.8	1.3	1.0	0.36	0.074	0.007	0.012	0.39	0.8
$\Delta R_{\tau\tau}^{\min(\max)}$	1.7	0.24	0.22	0.32	0.042	0.002	0.001	0.67	1.1
				$m_a = 30$ GeV					
$p_{T,b}$, ΔR_{bb}	8.4	34	81	6	2	0.72	1.4	0.063	0.72
m_{bb}	5.8	12	26	1.0	0.66	0.24	0.46	0.12	0.85
$p_{T,bb}$	5.8	11	25	1.0	0.63	0.23	0.44	0.13	0.86
$m_{4\tau}^{\mathrm{vis}}$	5.3	1.0	0.64	1.0	0.067	0.004	0.006	0.658	1.9
$\Delta R_{\tau\tau}^{\min(\max)}$	5.2	0.38	0.24	0.95	0.045	0.002	0.002	0.762	2.0
				$m_a = 40$ GeV					
$p_{T,b}$, ΔR_{bb}	10	34	81	7.3	2.0	0.72	1.4	0.074	0.87
m_{bb}	7.0	12	26	1.4	0.66	0.24	0.46	0.15	1.0
$p_{T,bb}$	6.9	11	25	1.4	0.63	0.23	0.44	0.15	1.0
$m_{4\tau}^{\mathrm{vis}}$	6.3	0.73	0.42	1.4	0.061	0.002	0.003	0.71	2.1
$\Delta R_{\tau\tau}^{\min(\max)}$	6.1	0.29	0.22	1.3	0.042	0.001	0.001	0.77	2.2
				$m_a = 50$ GeV					
$p_{T,b}$, ΔR_{bb}	11	34	81	8.4	2.0	0.72	1.4	0.082	0.96
m_{bb}	7.9	12	26	1.8	0.66	0.24	0.46	0.16	1.1
$p_{T,bb}$	7.8	11	25	1.7	0.63	0.23	0.44	0.16	1.1
$m_{4\tau}^{\mathrm{vis}}$	7.1	0.73	0.42	1.6	0.061	0.002	0.003	0.716	2.2
$\Delta R_{\tau\tau}^{\min(\max)}$	6.8	0.31	0.26	1.5	0.048	0.002	0.002	0.759	2.3
				$m_a = 60$ GeV					
$p_{T,b}$, ΔR_{bb}	13	34	81	10	2.0	0.72	1.4	0.094	1.1
m_{bb}	9.4	12	26	1.8	0.66	0.24	0.46	0.18	1.3
$p_{T,bb}$	9.3	11	25	1.8	0.63	0.23	0.44	0.19	1.3
$m_{4\tau}^{\mathrm{vis}}$	8.5	0.73	0.42	1.7	0.061	0.002	0.003	0.75	2.5
$\Delta R_{\tau\tau}^{\min(\max)}$	8.2	0.34	0.26	1.6	0.048	0.002	0.002	0.79	2.5

Owing to the complexity and limited statistics in the $pp \to hh \to 2b4\tau$ channel, it is of utmost importance to precisely explore all possible clues pertaining to beyond-SM interactions. In principle, new physics effects can potentially manifest through complex correlations between various input observables. The cut-based analysis, although robust, is susceptible to overlooking such multidimensional correlations. Accordingly, similar to Sec. II, we adopt the XGBoost algorithm as a multivariate technique with several kinematic observables,

$$\begin{aligned} &m_{hh}^{\rm vis}, \quad p_{T,hh}^{\rm vis}, \quad \Delta R_{hh}^{\rm vis}, \quad m_{T2}, \quad m_{T,h}, \quad m_{\rm eff}, \\ &p_{T,bb}, \quad m_{bb}, \quad \Delta R_{bb}, \quad m_{4\tau}^{\rm vis}, \\ &\Delta R_{\tau_1,\tau_2}, \quad \Delta R_{\tau_1,\tau_3}, \quad \Delta R_{\tau_1,\tau_4}, \quad \Delta R_{\tau_2,\tau_3}, \quad \Delta R_{\tau_2,\tau_4}, \\ &\Delta R_{\tau_3,\tau_4}, \quad \Delta R_{\tau\tau}^{\rm min}, \quad \Delta R_{\tau\tau}^{\rm max}. \end{aligned} \tag{3.1}$$

Here, $m_{hh}^{\rm vis}$ and $p_{T,hh}^{\rm vis}$ are the invariant mass and transverse momentum, respectively, for the visible components of the di-Higgs system, $\Delta R_{hh}^{\rm vis}$ is the distance in the $\eta - \phi$ plane between the reconstructed $h \to b\bar{b}$ and visible $h \to 4\tau$ system, $m_{\rm eff}$ is the effective mass of the di-Higgs system, $m_{\rm eff} = H_T + \not{E}_T$, and m_{T2} is motivated from Refs. [185,186]. The analysis in Refs. [185,186] illustrates the effectiveness of m_{T2} in estimating the mass of pair-produced particles in scenarios where both decay into visible and invisible components. The decay topology of the exotic scalars in our signal corresponds to a similar scenario as they are pair produced from the SM-like Higgs boson and undergo decay into visible and invisible candidates. The rest of the observables in Eq. (3.1) have their usual meanings.

The six most essential observables with the highest absolute SHAP values across all five signal benchmarks are $m_{4\tau}^{\rm vis}$, $\Delta R_{\tau\tau}^{\rm min}$, $\Delta R_{\tau\tau}^{\rm max}$, $m_{T,h}$, $\Delta R_{b\bar{b}}$, $m_{b\bar{b}}$. We note that the cut-and-count analysis discussed earlier was performed by optimizing the selection cuts on the first three observables on this list. For illustrative purposes, we present the distributions for the other three most important observables *viz* ΔR_{bb}, $m_{T,h}$, and m_{bb}, in Fig. 18, Appendix C.

The optimized signal and background yields from the XGBoost analysis, alongside the signal significance at the HL-LHC [for $\mathrm{Br}(h \to aa \to 4\tau) = 10\%$], without and with 5% systematic uncertainty, are presented in Table VIII. Compared to the cut-and-count analysis, the significance improves by $\mathcal{O}(25$–$45\%)$. Considering $\mathrm{Br}(h \to aa \to 4\tau) = 10\%$, the significance goes beyond 2. However, single Higgs production at the HL-LHC would be able to constrain $\mathrm{Br}(h \to aa \to 4\tau)$ up to ∼0.015% for $m_a = 60$ GeV (see Sec. II A). Considering the projection described above for exotic Higgs branching fraction, null signal events would be observed in the nonresonant di-Higgs channel at the HL-LHC at $\gtrsim 2$ s.d.

We next focus on the $\sqrt{s} = 100$ TeV hadron collider FCC-hh. The di-Higgs production cross section is ∼30 times greater than that at the HL-LHC, which motivates us to investigate the prospects for exotic Higgs decay. We consider the same background processes as above. We use the FCC-hh detector card of DELPHES [187] for the detector simulation with b-tagging, c, and light jet mistagging efficiencies as functions of p_T, as prescribed in Appendix A of [187]. For our analysis, the typical p_T of a jet is much less than the TeV scale. Hence, the b-tagging, c-mistagging, and light jet mistagging efficiencies are approximately 85%, 5%, and 1%, respectively. Jets are reconstructed from particle-flow objects using FastJet with $R = 0.3$ and $p_T > 30$ GeV. The basic trigger and selection cuts on the final state objects remain unchanged.

TABLE VIII. Signal and background yields, and signal significance, at the HL-LHC from XGBoost analysis in the $pp \to hh \to (h \to b\bar{b})(h \to aa \to 4\tau)$ channel. The results shown here have been derived for $\mathrm{Br}(h \to aa \to 4\tau) = 10\%$.

$\sqrt{s}$ (TeV)	m_a (GeV)	Total background yield, B	Signal efficiency ($\times 10^{-4}$)	Signal yield, S	Significance (5% systematic)
14	20	1.8	2.5	3.2	1.4 (1.4)
	30	2.7	6.7	8.6	2.6 (2.6)
	40	3.8	8.4	10	2.8 (2.8)
	50	4.5	9.3	12	2.9 (2.9)
	60	5.0	11	14	3.2 (3.2)

Figure 9 shows the distributions of $\Delta R^{\rm min}$, $\Delta R^{\rm max}$, and $m_{4\tau}^{\rm vis}$ variables. The peak in the $\Delta R^{\rm min} < 0.3$ region is higher for $\sqrt{s} = 100$ TeV because here the τ objects are more boosted, and the decay products are more collimated than at $\sqrt{s} = 14$ TeV. Table IX shows the optimized cuts on these variables.

Using these cuts, we perform a cut-and-count analysis. The cut-flow information, along with the signal significance, is presented in Table X. Assuming a 10% branching of $h \to 4\tau$, we observe a much higher signal yield and signal significance at the $\sqrt{s} = 100$ TeV collider. At the FCC-hh, we obtain signal significance of 24,48,50,54, and 50 for $m_a = 20$, 30, 40, 50, and 60 GeV, respectively. We also apply the XGBoost analysis using the observables in Eq. (3.1). Table XI shows the signal efficiency, signal and background yields, and signal significance with and without 5% systematic uncertainty. As expected, the multivariate method resulted in $\mathcal{O}(30$–$45\%)$ improvement in the signal significance.[5]

The signal significance at FCC-hh is ∼76 s.d. for $m_a = 60$ GeV with $\mathrm{Br}(h \to aa \to 4\tau) = 10\%$. The significance at FCC-hh drops by $\mathcal{O}(24\%)$ to ∼58 s.d. on introducing a 5% systematic uncertainty. Adopting the HL-LHC reach for exotic Higgs branching ratio at $m_a = 60$ GeV from

[5]Appendix D (see Table XX) lists the results of XGBOOST analysis with jet radius $R = 0.4$ instead of 0.3.

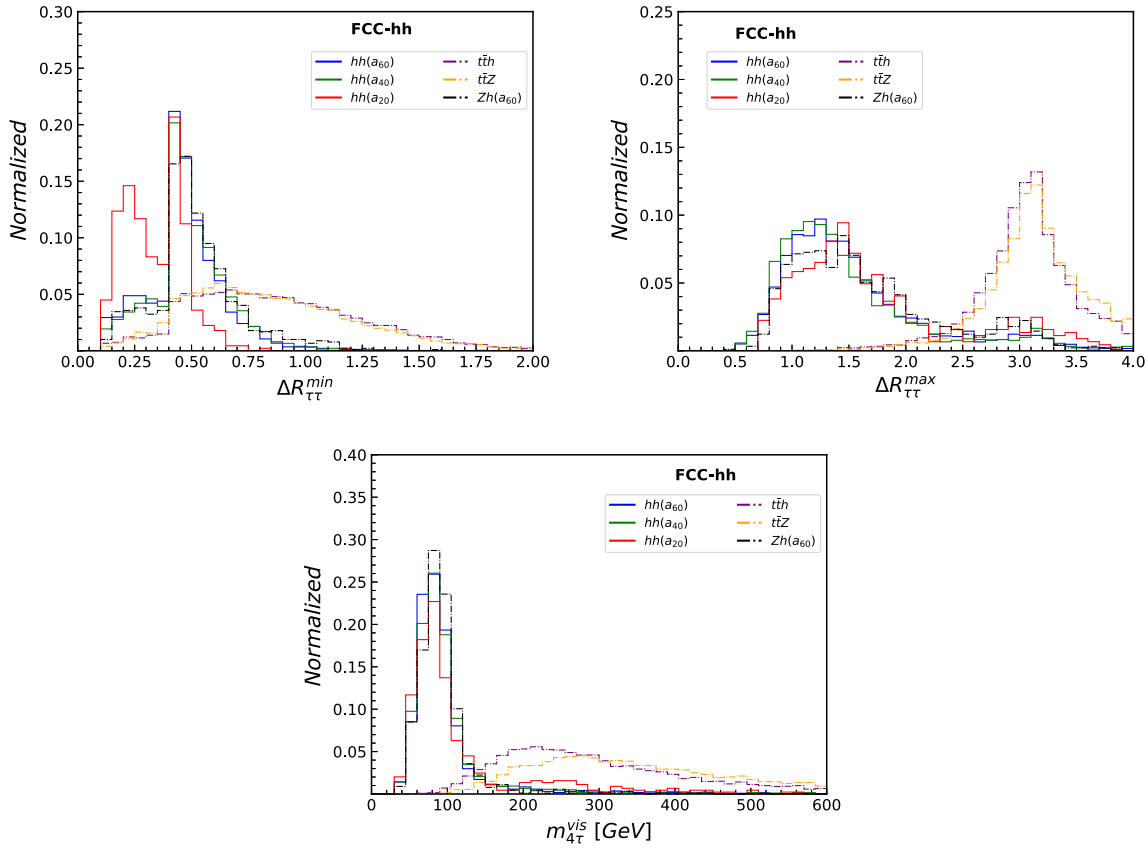

FIG. 9. Distributions of $\Delta R_{\tau\tau}^{\min}$, $\Delta R_{\tau\tau}^{\max}$, and $m_{4\tau}^{\mathrm{vis}}$ for signal benchmarks $m_a = 20, 40, 60$ GeV, and dominant backgrounds, in the $pp \to hh \to (h \to b\bar{b})(h \to aa \to 4\tau)$ channel at $\sqrt{s} = 100$ TeV LHC.

searches in the single Higgs production channel (see Fig. 4), $\mathrm{Br}(h \to aa \to 4\tau) \sim 0.015\%$, the significance at FCC-hh drops to <1 s.d. However, it must be noted that if a light scalar of mass 60 GeV is first observed at the HL-LHC, there remains the possibility for a 5 s.d. discovery at the FCC-hh through the Higgs pair production channel, provided $\mathrm{Br}(h \to aa \to 4\tau) \gtrsim 1\%$. Overall, prospects at the $\sqrt{s} = 100$ TeV collider look promising, and it might be possible to access exotic Higgs decays in $pp \to hh$ searches at the FCC-hh.

Current measurements from CMS in the combined $b\bar{b}ZZ$, *multilepton*, $b\bar{b}\gamma\gamma$, $b\bar{b}\tau\tau$, and $b\bar{b}b\bar{b}$ channels [57] and ATLAS in the combined $b\bar{b}\gamma\gamma$, $b\bar{b}\tau\tau$, and $b\bar{b}b\bar{b}$ channels [58] have imposed constraints on the di-Higgs signal strength, limiting it to $\mu_{hh} < 3.4$ and 2.4 at 95% CL, respectively. For the sake of completeness, we translate the results from cut-and-count (Tables VII and X) and XGBoost analyses (Tables VIII and XI) into upper limit projections on the di-Higgs signal strength μ_{hh}^{ggF} as a function of $\mathrm{Br}(h \to aa \to 4\tau)$, as shown in Fig. 10. The solid lines represent the projected upper limits when systematic uncertainties are not considered. We observe that the HL-LHC would be able to probe exotic Higgs decays up to $\mathrm{Br}(h \to aa \to 4\tau) \sim 7\%$ for $m_a = 60$ GeV through cut-and-count analysis in the nonresonant di-Higgs production channel, at 95% CL. Upon using XGBoost, the projected sensitivity improves only to $\mathrm{Br}(h \to aa \to 4\tau) \sim 5\%$. The potential reach at the

TABLE IX. Basic selection and optimized cuts imposed in the cut-and-count analysis for $pp \to hh \to (h \to b\bar{b})(h \to aa \to 4\tau)$ channel at the FCC-hh.

Basic selection cuts
$p_{T,b_1(b_2)} > 40(30)$ GeV, $0.4 < \Delta R_{bb} < 2.0$
90 GeV $< m_{bb} <$ 130 GeV
$p_{T,bb} > 80$ GeV
Optimized cuts for 100 TeV analysis
$m_{4\tau}^{\mathrm{vis}} < [200, 200, 170, 170, 150]$ GeV for $m_a = [20, 30, 40, 50, 60]$ GeV
$\Delta R_{\tau\tau}^{\min} < [0.8, 0.9, 0.9, 1.0, 1.0]$ and $\Delta R_{\tau\tau}^{\max} < [2.1, 2.4, 2.4, 4.0, 4.0]$ for $m_a = [20, 30, 40, 50, 60]$ GeV

TABLE X. Signal and background yields in the $pp \to hh \to (h \to b\bar{b})(h \to aa \to 4\tau)$ channel, at each step of the cut-based analysis for the signal benchmarks $m_a = 20$, 30, 40, 50, and 60 GeV and the dominant backgrounds at the FCC-hh. Signal significance at the FCC-hh is also shown for $\mathrm{Br}(h \to aa \to 4\tau) = 10\%$.

	Event rates at $\sqrt{s} = 100$ TeV with $\mathcal{L} = 30$ ab^{-1}								
		Backgrounds							
Cut flow	Signal	$t\bar{t}h$	$t\bar{t}Z$	Zh	$4\ell 2b$	$t\bar{t}ZZ$	$t\bar{t}WW$	$\frac{S}{(S+B)}$	Significance
				$m_a = 20$ GeV					
$p_{T,b}$, ΔR_{bb}	1609	23454	39799	505	736	601	1497	0.024	6.2
m_{bb}	1215	7098	11089	67	195	163	374	0.060	8.6
$p_{T,bb}$	1208	6908	10683	67	188	158	364	0.062	8.6
$m_{4\tau}^{\mathrm{vis}}$	972	1779	889	59	44	14	29	0.26	16
$\Delta R_{\tau\tau}^{\mathrm{min(max)}}$	887	190	193	49	17	3.8	2.0	0.66	24
				$m_a = 30$ GeV					
$p_{T,b}$, ΔR_{bb}	4362	23454	39799	973	736	601	1497	0.061	16
m_{bb}	3222	7098	11089	122	195	163	374	0.14	22
$p_{T,bb}$	3211	6908	10684	122	188	158	364	0.15	22
$m_{4\tau}^{\mathrm{vis}}$	2814	915	425	118	29	8.1	13	0.65	43
$\Delta R_{\tau\tau}^{\mathrm{min(max)}}$	2748	190	193	116	20	3.6	3.0	0.84	48
				$m_a = 40$ GeV					
$p_{T,b}$, ΔR_{bb}	4909	23454	39799	1201	736	601	1497	0.068	18
m_{bb}	3578	7098	11089	142	195	163	374	0.16	24
$p_{T,bb}$	3554	6908	10684	140	188	158	364	0.16	24
$m_{4\tau}^{\mathrm{vis}}$	3112	915	425	126	29	8.1	13	0.67	46
$\Delta R_{\tau\tau}^{\mathrm{min(max)}}$	2999	189	193	124	20	3.6	3.0	0.85	50
				$m_a = 50$ GeV					
$p_{T,b}$, ΔR_{bb}	5396	23454	39799	1223	736	601	1497	0.074	20
m_{bb}	4026	7098	11089	146	195	163	374	0.17	26
$p_{T,bb}$	3995	6908	10684	146	188	158	364	0.18	27
$m_{4\tau}^{\mathrm{vis}}$	3454	363	193	124	19	4.3	6.0	0.83	54
$\Delta R_{\tau\tau}^{\mathrm{min(max)}}$	3450	276	193	122	18	3.8	4.0	0.85	54
				$m_a = 60$ GeV					
$p_{T,b}$, ΔR_{bb}	6591	23454	39799	1608	736	601	1497	0.089	24
m_{bb}	4829	7098	11089	168	195	163	374	0.20	31
$p_{T,bb}$	4801	6908	10684	168	188	158	364	0.21	31
$m_{4\tau}^{\mathrm{vis}}$	4083	363	193	158	19	4.3	6.0	0.85	59
$\Delta R_{\tau\tau}^{\mathrm{min(max)}}$	4083	276	193	156	18	3.8	4.0	0.86	59

TABLE XI. Signal and background yields, and signal significance, at the FCC-hh from XGBoost analysis in the $pp \to hh \to (h \to b\bar{b})(h \to aa \to 4\tau)$ channel. The results shown here have been derived for $\mathrm{Br}(h \to aa \to 4\tau) = 10\%$.

$\sqrt{s}$ (TeV)	m_a (GeV)	Total background yield, B	Signal efficiency ($\times 10^{-4}$)	Signal yield, S	Significance (5% systematic)
100	20	716	4.1	1749	35 (28)
	30	1125	10.7	4595	61 (49)
	40	1247	13	5521	67 (53)
	50	1384	14	5995	70 (54)
	60	1565	16	7015	76 (58)

FCC-hh is more than an order of magnitude stronger than at the HL-LHC. For $m_a = 60$ GeV, FCC-hh would be able to probe $\mathrm{Br}(h \to aa \to 4\tau)$ as small as ∼0.1% and 0.07% at 95% CL through the cut-and-count and machine-learning based XGBoost analysis, respectively.

However, as discussed earlier, these limits are almost an order of magnitude weaker than the projections from single Higgs search channels considered in Sec. II. Having exhausted the discovery prospects for exotic Higgs decay in the Higgs pair production channel, we focus on other possible Higgs production modes. The $b\bar{b}4\tau$ final state considered in the present section can also manifest in Z associated Higgs production $pp \to (Z \to b\bar{b})h$, which is precisely the goal for our next section.

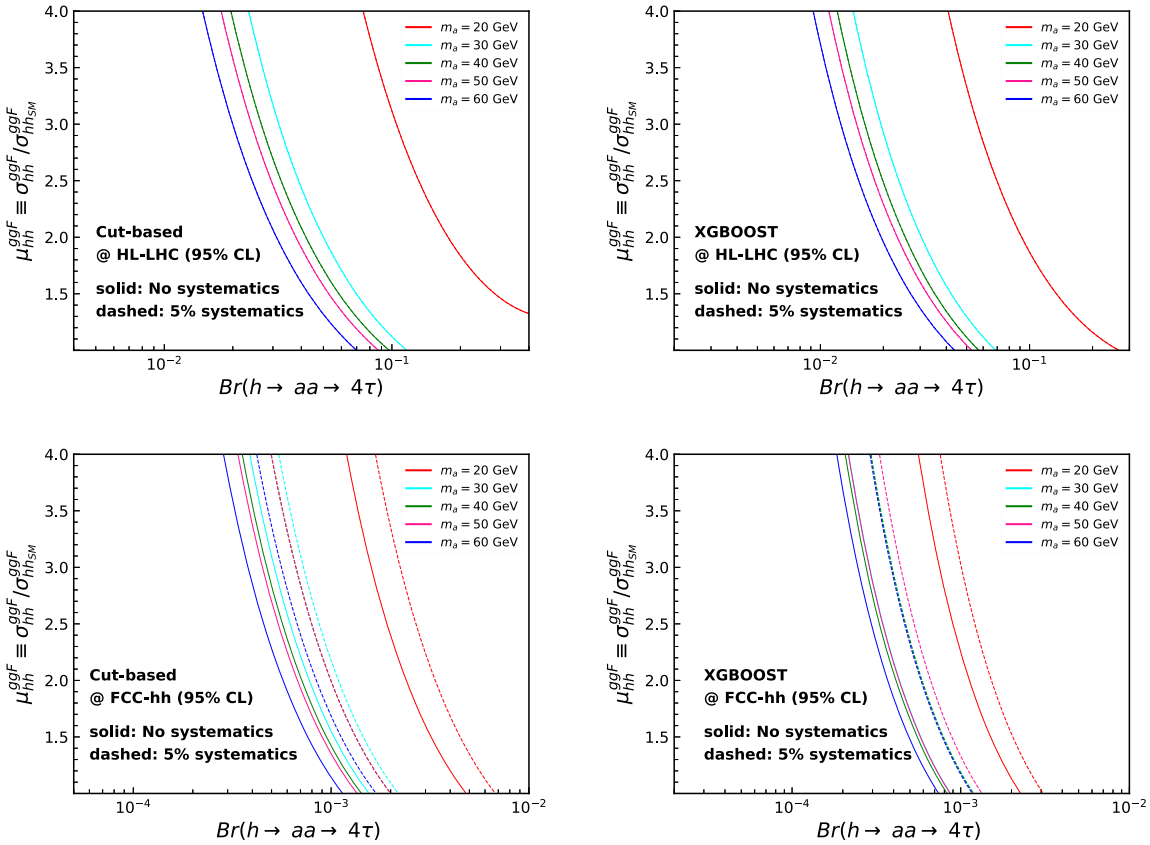

FIG. 10. Signal strength factor at 95% CL for the nonresonant Higgs pair production with respect to $\mathrm{Br}(h \to aa \to 4\tau)$ at $\sqrt{s} = 14$ TeV with $\mathcal{L} = 3$ ab^{-1} (top panel) and $\sqrt{s} = 100$ TeV with $\mathcal{L} = 30$ ab^{-1} (bottom panel). On the left, results from cut-based analysis are shown. The XGBoost results are shown on the right.

IV. HIGGS-STRAHLUNG: $pp \to Zh \to (Z \to b\bar{b})(h \to aa \to 4\tau)$

Higgs-strahlung production $pp \to Zh$, with $Z \to b\bar{b}$ and $h \to aa \to 4\tau$, served as a major background for the nonresonant di-Higgs signal considered in Sec. III. An alternate point of view would be to consider the Zh process with the h decaying exotically as a signal by itself, and the di-Higgs process would be a potential background. We analyze such a case in the present section. The background processes are similar to those considered in Sec. III barring $pp \to Zh$ which is adopted as the signal process here. The new addition to the list of backgrounds is nonresonant di-Higgs production $pp \to hh \to (h \to b\bar{b}) \times (h \to aa \to 4\tau)$.

We closely follow the analysis strategy adopted for the nonresonant di-Higgs channel considered in Sec. III, with relatively smaller thresholds on the invariant mass and transverse momentum for the $b\bar{b}$ pairs. The Z boson is reconstructed by constraining $m_{b\bar{b}} \in [50, 100]$ GeV and $p_{T,b\bar{b}}$ is required to be $p_{T,b\bar{b}} > 50$ GeV. We first perform a cut-and-count analysis to estimate the projected sensitivity at the HL-LHC by optimizing the selection cuts on $m_{4\tau}^{\mathrm{vis}}$, $\Delta R_{\tau\tau}^{\mathrm{min}}$ and $\Delta R_{\tau\tau}^{\mathrm{max}}$. The optimization is performed for five signal benchmarks considered in Sec. II. The basic selection cuts and the optimized cuts on $m_{4\tau}^{\mathrm{vis}}$, $\Delta R_{\tau\tau}^{\mathrm{min}}$, and $\Delta R_{\tau\tau}^{\mathrm{max}}$ for different signal benchmarks are summarized in Table XII. The cut-flow information and signal significance at the HL-LHC are shown in Table XIII. Here again, we have assumed $\mathrm{Br}(h \to aa \to 4\tau) = 10\%$. At $m_a = 20(60)$ GeV, we obtain significance of 1.06 (2.36) at 5 s.d. uncertainty. It must be noted that the significance values computed for the Zh signal are roughly comparable with the results from searches in the nonresonant di-Higgs channel (cf. Sec. III).

We also perform the XGBoost analysis using the kinematic observables in Eq. (3.1). The subset of training observables with the highest importance rankings is similar to that for the nonresonant di-Higgs channel. We present the corresponding signal and background yields, signal efficiency, and signal significance with and without systematic uncertainty ($\sigma_{\mathrm{unc}} = 5\%$), at the HL-LHC, in Table XIV. Here again, we consider $\mathrm{Br}(h \to aa \to 4\tau) = 10\%$ while computing the signal yields and the background yield for $pp \to hh$. Our results are also translated into projected upper limits on $\mu_{Zh} = \sigma_{Zh}/\sigma_{Zh}^{\mathrm{SM}}$ and $\mathrm{Br}(h \to aa \to 4\tau)$ as shown in Fig. 11. We observe that the HL-LHC would be able to probe

TABLE XII. Basic selection and optimized cuts imposed in the cut-and-count analysis for $pp \to Zh \to (Z \to b\bar{b})(h \to aa \to 4\tau)$ channel.

Cuts applied for 14 TeV analysis of $Zh \to b\bar{b}4\tau$
$p_{T,b_1(b_2)} > 30\,(20)$ GeV, $0.4 < \Delta R_{bb} < 2.0$
$50\ \text{GeV} < m_{bb} < 100\ \text{GeV}$
$p_{T,bb} > 50$ GeV
$m_{4\tau}^{\text{vis}} < [125, 120, 120, 120, 120]$ GeV for $m_a = [20, 30, 40, 50, 60]$ GeV
$\Delta R_{\tau\tau}^{\text{min}} < [0.7, 0.9, 1.2, 1.2, 1.2]$ and $\Delta R_{\tau\tau}^{\text{max}} < 3.5$ for $m_a = [20, 30, 40, 50, 60]$ GeV

TABLE XIII. Signal and background yields in the $pp \to (Z \to b\bar{b})(h \to aa \to 4\tau)$ channel, at each step of the cut-based analysis for the signal benchmarks $m_a = 20$, 30, 40, 50, and 60 GeV and the dominant backgrounds at the HL-LHC. The signal significance at the HL-LHC is also shown for $\text{Br}(h \to aa \to 4\tau) = 10\%$.

	Event rates at $\sqrt{s} = 14$ TeV with $\mathcal{L} = 3$ ab^{-1}								
		Backgrounds							
Cut flow	Signal	$t\bar{t}h$	$t\bar{t}Z$	hh	$4\ell 2b$	$t\bar{t}ZZ$	$t\bar{t}WW$	$\frac{S}{(S+B)}$	Significance
				$m_a = 20$ GeV					
$p_{T,b}$, ΔR_{bb}	2.3	34	82	2.3	2.8	0.73	1.4	0.022	0.25
m_{bb}	2.2	17	38	2.2	1.1	0.30	0.6	0.037	0.29
$p_{T,bb}$	2.2	17	38	2.2	1.1	0.30	0.59	0.037	0.29
$m_{4\tau}^{\text{vis}}$	2.1	0.85	0.55	0.94	0.09	0.003	0.010	0.46	0.99
$\Delta R_{\tau\tau}^{\text{min(max)}}$	2.1	0.49	0.28	0.94	0.08	0.005	0.006	0.54	1.1
				$m_a = 30$ GeV					
$p_{T,b}$, ΔR_{bb}	6.2	35	82	8.4	2.1	0.73	1.4	0.046	0.53
m_{bb}	6.0	17	38	3.3	1.2	0.30	0.60	0.089	0.73
$p_{T,bb}$	6.0	17	38	3.3	1.2	0.29	0.59	0.090	0.73
$m_{4\tau}^{\text{vis}}$	5.6	0.72	0.48	2.9	0.090	0.001	0.008	0.57	1.8
$\Delta R_{\tau\tau}^{\text{min(max)}}$	5.5	0.56	0.33	2.9	0.090	0.001	0.006	0.59	1.8
				$m_a = 40$ GeV					
$p_{T,b}$, ΔR_{bb}	7.3	34	82	10	2.1	0.73	1.4	0.053	0.62
m_{bb}	7.0	17	38	3.9	1.2	0.30	0.60	0.10	0.84
$p_{T,bb}$	7.0	17	38	3.9	1.2	0.30	0.59	0.10	0.84
$m_{4\tau}^{\text{vis}}$	6.5	0.72	0.48	3.4	0.090	0.001	0.008	0.58	1.9
$\Delta R_{\tau\tau}^{\text{min(max)}}$	6.5	0.67	0.42	3.4	0.090	0.001	0.008	0.58	1.9
				$m_a = 50$ GeV					
$p_{T,b}$, ΔR_{bb}	8.5	34	82	11	2.1	0.73	1.45	0.06	0.72
m_{bb}	8.1	17	38	4.5	1.2	0.30	0.60	0.11	0.97
$p_{T,bb}$	8.1	17	38	4.5	1.2	0.30	0.59	0.12	0.97
$m_{4\tau}^{\text{vis}}$	7.6	0.72	0.48	4.1	0.090	0.001	0.008	0.58	2.1
$\Delta R_{\tau\tau}^{\text{min(max)}}$	7.5	0.67	0.42	4.1	0.090	0.001	0.008	0.59	2.1
				$m_a = 60$ GeV					
$p_{T,b}$, ΔR_{bb}	10	35	82	14	2.1	0.73	1.45	0.071	0.86
m_{bb}	9.9	17	38	5.2	1.2	0.30	0.60	0.14	1.16
$p_{T,bb}$	9.8	17	38	5.2	1.2	0.30	0.59	0.14	1.15
$m_{4\tau}^{\text{vis}}$	9.2	0.72	0.48	4.7	0.090	0.001	0.008	0.61	2.4
$\Delta R_{\tau\tau}^{\text{min(max)}}$	9.2	0.67	0.42	4.7	0.090	0.001	0.008	0.61	2.4

$\text{Br}(h \to aa \to 4\tau)$ up to only ~5% at 95% CL uncertainty for $m_a = 60$ GeV through searches in the SM Higgs-strahlung production channel. We would like to note that the projected sensitivity for $\text{Br}(h \to aa \to 4\tau)$ from searches in the Zh channel is comparable to that of the Higgs pair production channel considered in Sec. III, and weaker compared to other single Higgs production channels in Sec. II.

TABLE XIV. Signal and background yields, and signal significance, at the HL-LHC from XGBoost analysis in the $pp \to Zh \to (Z \to b\bar{b})(h \to aa \to 4\tau)$ channel. The results assume Br $(h \to aa \to 4\tau) = 10\%$.

$\sqrt{s}$ (TeV)	m_a (GeV)	Total background yield, B	Signal efficiency ($\times 10^{-4}$)	Signal yield, S	Significance (5% systematic)
14	20	1.5	0.7	2.7	1.3 (1.3)
	30	3.0	1.7	6.4	2.1 (2.1)
	40	3.3	2.0	7.4	2.3 (2.3)
	50	4.7	2.4	9.0	2.4 (2.4)
	60	5.2	3.0	11	2.8 (2.8)

V. RESONANT HIGGS PAIR PRODUCTION: $pp \to H \to hh \to (h \to b\bar{b})(h \to aa \to 4\tau)$

The reach of nonresonant di-Higgs searches is limited mainly due to its smaller production rate. In general, the sensitivity in di-Higgs channels could benefit from an enhancement in production cross section. One such possibility is presented by resonant Higgs pair production, where the SM-like Higgs boson pair is produced from the decay of a directly produced heavy scalar, H. Exotic Higgs searches in the resonant di-Higgs channel are also relevant in extending/complementing the coverage of the BSM landscape since the extended Higgs sector in several well-motivated BSM frameworks entail such a heavy Higgs boson alongside an exotic light Higgs viz., next-to-minimal supersymmetric standard model (NMSSM) [188,189], 2HDM + S [190], among other models.

In this section, we explore the HL-LHC prospects of exotic Higgs searches in the resonant di-Higgs channel. We restrict to the final state considered in Sec. III and analyze the signal process: $pp \to H \to hh \to (h \to b\bar{b})(h \to aa \to 4\tau)$. Along with the background processes in Sec. III, we also consider the nonresonant Higgs pair production process: $pp \to hh \to (h \to b\bar{b})(h \to aa \to 4\tau)$ as a BSM background. The basic selection criteria imposed in Sec. III are also applied here. We consider four benchmark values of heavy Higgs mass, $m_H = 300$, 500, 800, and 1000 GeV and three light scalar mass choices, $m_a = 20$, 40, and 60 GeV, for each value of m_H. We perform an XGBoost analysis for these specific choices of $\{m_H, m_a\}$ using the observables in Eq. (3.1) and translate the results into model-independent projected upper limits on $\sigma(pp \to H \to hh)$ as a function of m_H. Two important observables in the multivariate analysis are $\Delta R_{\tau\tau}^{\min}$ and $m_{4\tau}^{\rm vis}$. In Fig. 12, we illustrate $\Delta R_{\tau\tau}^{\min}$ and $m_{4\tau}^{\rm vis}$ distributions for several signal benchmarks $\{m_H = 300, 500, 800, 1000$ GeV, $m_a = 20, 40, 60$ GeV$\}$ and dominant backgrounds, at $\sqrt{s} = 14$ TeV LHC. For brevity, we are not showing the remaining important observables. The $\Delta R_{\tau\tau}^{\min}$ distribution shifts towards smaller values with decreasing m_a. The exotic scalars are produced with a larger boost in case of low m_a, leading to more collimated decay products. For instance, the peak of $\Delta R_{\tau\tau}^{\min}$ distribution is much higher in the $\Delta R < 0.4$ region for $m_a = 20$ GeV, especially when $m_H = 1000$ GeV.

In Table XV, we present the signal efficiency and background yields at the HL-LHC, from the XGBoost analysis. As discussed earlier in Secs. II A and III, the signal efficiency falls with decreasing m_a. It must also be noted that for a given m_a, signal efficiency improves with increasing m_H, except when $m_H = 1000$ GeV. This happens because the SM-like Higgs bosons are produced with a relatively more considerable boost for higher m_H, resulting in an overall shift towards the kinematic region farther away from the SM backgrounds. However, the decay products become too collimated for very high $m_H \sim 1000$ GeV, which becomes challenging to resolve.

We translate the optimized signal efficiencies, ϵ_S, and background yields B, to model-independent projected upper limits on the resonant di-Higgs production cross section $\sigma(pp \to H \to hh)_{UL}$,

$$\sigma(pp \to H \to hh)_{UL} = \frac{\eta_S \cdot \sqrt{B}}{\epsilon_S \cdot \mathcal{L} \cdot \mathrm{Br}(h \to b\bar{b})_{\rm SM} \cdot \mathrm{Br}(h \to aa \to 4\tau) \cdot 2}. \quad (5.1)$$

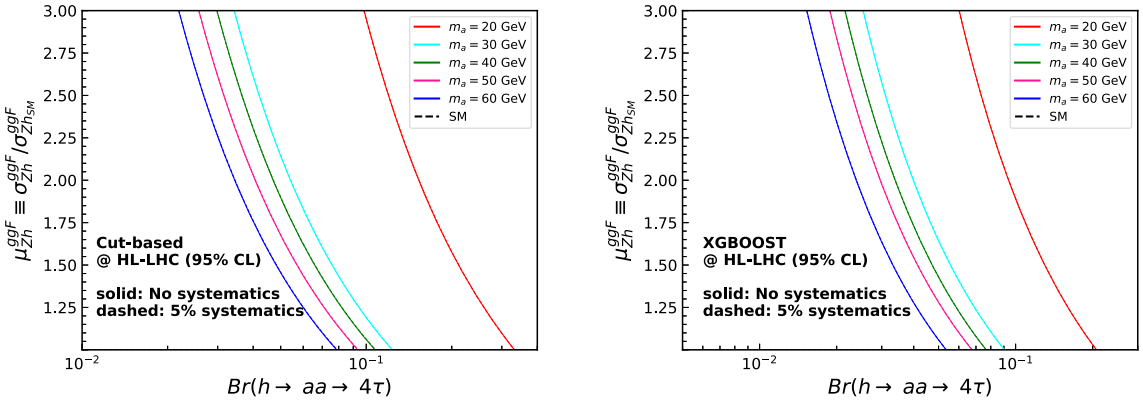

FIG. 11. Signal strength factor in the $pp \to Zh \to (Z \to b\bar{b})(h \to aa \to 4\tau)$ channel at 95% CL vs Br$(h \to aa \to 4\tau)$ at the HL-LHC for the cut-based (left panel) and XGBoost (right panel) analysis.

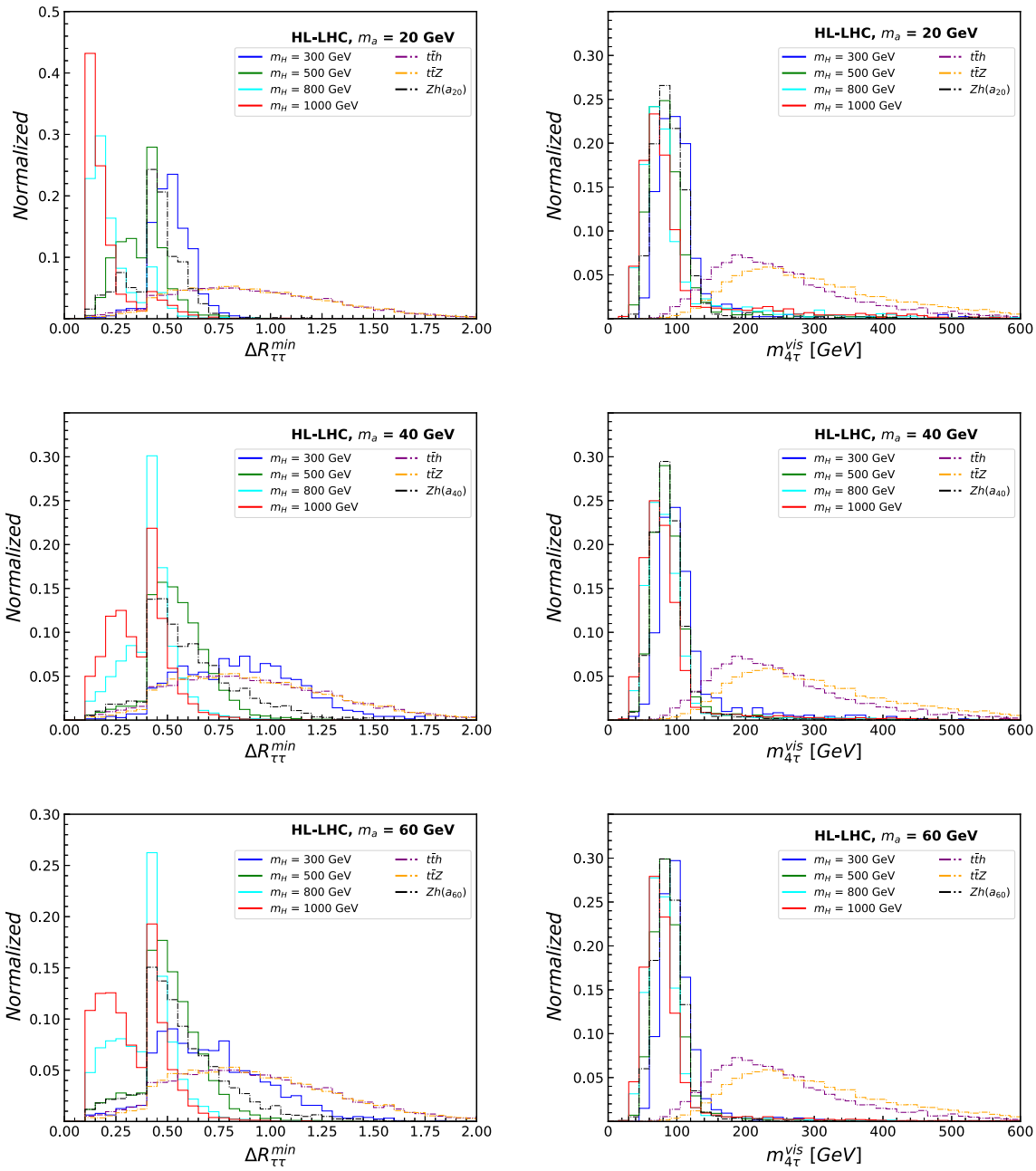

FIG. 12. Distributions of $\Delta R_{\tau\tau}^{\min}$ (left), and $m_{4\tau}^{\rm vis}$ (right) for signal benchmarks $m_a = 20$ GeV (top row), $m_a = 40$ GeV (middle row) and $m_a = 60$ GeV (bottom row), and dominant backgrounds, in the $pp \to H \to hh \to (h \to b\bar{b})(h \to aa \to 4\tau)$ channel, at $\sqrt{s} =$ 14 TeV LHC. The mass of heavy Higgs boson $m_H = 300$, 500, 800, 1000 GeV.

Here η_S represents the standard deviation from the background. In the present analysis, we derive the projected upper limits at $\eta_S = 2$, which corresponds to a 95% confidence interval, with $\mathrm{Br}(h \to b\bar{b}) = 58\%$ [191] and $\mathrm{Br}(h \to aa \to 4\tau) = 10\%$ [2,32].

In Fig. 13, we present $\sigma(pp \to H \to hh)_{UL}$ as a function of m_H for three light Higgs mass scenarios, $m_a = 20$, 40, and 60 GeV. These projections demonstrate the future sensitivity of resonant di-Higgs searches in the $pp \to H \to hh \to (h \to b\bar{b})(h \to aa \to 4\tau)$ channel at the HL-LHC. We observe that at $m_H = 300$ GeV, HL-LHC would be able to probe resonant di-Higgs production cross sections up to $\sigma(pp \to H \to hh) \gtrsim 65, 46, 29$ fb for exotic scalar of mass, $m_a = 20$, 40, 60 GeV, respectively, for $\mathrm{Br}(h \to aa \to 4\tau) = 10\%$, at 95% CL. We observe that the projected sensitivity gets stronger with increasing m_H up to $m_h \sim 800$ GeV, after which the upper limit remains almost unchanged.

Figure 14 shows the $\sigma(pp \to H \to hh)_{UL}$ as a function of $\mathrm{Br}(h \to aa \to 4\tau)$ following Eq. (5.1). This section

TABLE XV. Signal efficiency and background yields from XGBoost analysis in the $pp \to H \to hh \to (h \to b\bar{b})(h \to aa \to 4\tau)$ channel at the HL-LHC. Results are derived for $\mathrm{Br}(h \to aa \to 4\tau) = 10\%$.

$pp \to H \to hh \to b\bar{b}aa \to 2b4\tau$, $\sqrt{s} = 14$ TeV										
Masses (GeV)		Background yield at 3 ab^{-1}								
m_H	m_a	$t\bar{t}h$	$t\bar{t}Z$	Zh	hh	$4\ell 2b$	$t\bar{t}ZZ$	$t\bar{t}WW$	Total	Signal efficiency ($\times 10^{-4}$)
300	20	0.24	0.11	0.52	0.31	0.096	0.001	0.004	1.3	0.99
	40	0.31	0.20	0.54	0.42	0.102	0.006	1.006	1.6	1.5
	60	0.34	0.11	0.85	0.65	0.12	0.001	0.006	2.1	2.8
500	20	0.21	0.088	0.54	1.5	0.074	0.003	0.005	2.4	3.1
	40	0.28	0.18	1.7	5.9	0.083	0.005	0.007	8.2	12
	60	0.21	0.15	1.6	6.8	0.070	0.003	0.004	8.9	15
800	20	0.15	0.088	0.36	0.68	0.15	0.004	0.012	1.4	3.5
	40	0.098	0.13	1.4	2.0	0.11	0.005	0.008	3.8	17
	60	0.098	0.13	1.5	2.6	0.14	0.008	0.006	4.5	19
1000	20	0.049	0.044	0.18	0.25	0.090	0.003	0.005	0.62	2.8
	40	0.049	0.044	0.58	0.94	0.12	0.008	0.010	1.7	13
	60	0.082	0.088	0.62	1.1	0.13	0.007	0.009	2.0	13

focuses on resonant di-Higgs production with an exotically decaying SM-like Higgs boson. The literature has also explored scenarios where SM-like Higgs bosons decay via SM modes. For example, both CMS and ATLAS collaborations have performed resonant di-Higgs searches in the $H \to hh \to b\bar{b}b\bar{b}$ [192], $b\bar{b}\tau^+\tau^-$ [193], and $b\bar{b}\gamma\gamma$ [194] final states using the 13 TeV LHC data collected at $\mathcal{L} \sim 139$ fb^{-1}, and derived upper bounds on $\sigma(pp \to H \to hh)$. A similar variation of these current upper limits at 95% CL on $\sigma(pp \to H \to hh)$ with BSM $\mathrm{Br}(h \to aa \to 4\tau)$ have been drawn in black.

For a 300 GeV heavy Higgs, the current searches have ruled out up to $\sigma \sim 300$ fb for $\mathrm{Br}(h \to aa \to 4\tau) \sim 0.5\%$ at 95% CL. With increasing mass of the heavy Higgs, the region becomes much more constrained by current limits. For $m_H = 1000$ GeV, HL-LHC will be sensitive to $\sigma(pp \to H \to hh)$ up to 8 fb for $\mathrm{Br}(h \to aa \to 4\tau) \sim 7\%$.

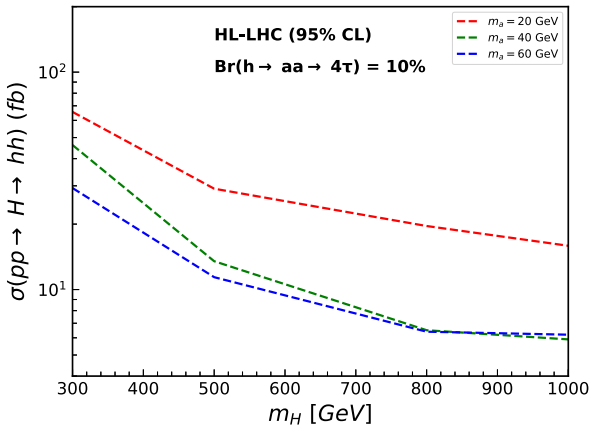

FIG. 13. Projected upper limits at 95% CL on $\sigma(pp \to H \to hh)$ as a function of m_H from resonant di-Higgs searches in the $b\bar{b}4\tau$ final state at the HL-LHC, assuming $\mathrm{Br}(h \to aa \to 4\tau) = 10\%$. The red, green, and blue lines correspond to different light scalar masses, $m_a = 20$, 40, and 60 GeV, respectively.

In Fig. 15 (left), we show the current upper limits from experiments for different masses of heavy Higgs with dashed lines. The projected sensitivity in the decay modes above at the HL-LHC has also been studied in Ref. [131]. We display the projected upper limits at the HL-LHC in the $b\bar{b}b\bar{b}$ and $b\bar{b}\gamma\gamma$ channel in Fig. 15 (right) with dashed colored lines and contrast them with the findings of the present analysis where resonant di-Higgs production is probed in exotic final states. For this purpose, we consider the $m_a = 60$ GeV scenario, which furnishes the most robust limits among other signal benchmarks considered in the present work. In Fig. 15 (right), we present the projected upper limits derived in the current analysis in solid black. The results indicate that the projected sensitivity for resonant di-Higgs searches in exotic final state assuming a saturated decay branching of $\mathrm{Br}(h \to aa \to 4\tau) = 10\%$ is almost comparable if not slightly stronger than the $4b$ and $2b2\gamma$ channel at the HL-LHC. We further compare the limits with the upper bounds from current LHC runs by rescaling our HL-LHC projections (see Fig. 13) to the current LHC luminosity ($\mathcal{L} = 139$ fb^{-1}) in Fig. 15 (left). Below $m_H \lesssim 500$ GeV, upper limits from the $2b4\tau$ channel considered in the present section are almost comparable to the $2b2\tau$ channel. At higher heavy Higgs masses $m_H \gtrsim 650$ GeV, limits from the $4b$ channel begin to dominate. At $m_H \sim 1$ TeV, the upper limits from the present analysis are roughly 2–5 times weaker than the $4b$ channel.

We briefly study the resonant production of a pair of exotic light scalars from a heavy Higgs. In this case, the final state consists of 4τs. Hence, we follow a similar

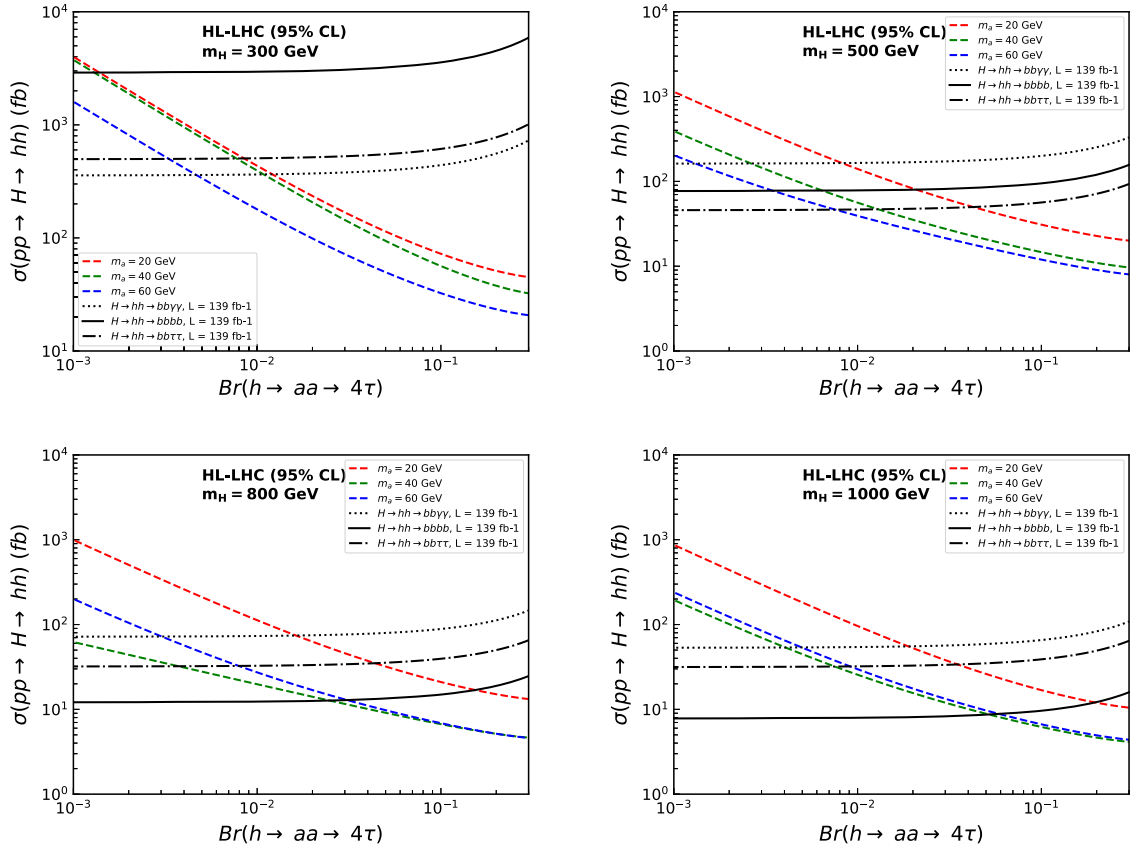

FIG. 14. Variation of the projected upper limits at 95% CL on $\sigma(pp \to H \to hh)$ as a function of $\mathrm{Br}(h \to aa \to 4\tau)$ for $m_H = 300$, 500, 800, 1000 GeV at the HL-LHC. The red, green, and blue lines correspond to different light scalar masses, $m_a = 20$, 40, and 60 GeV, respectively. Variation of the current upper limits at 95% CL on $\sigma(pp \to H \to hh)$, from resonant di-Higgs searches in $b\bar{b}b\bar{b}$ [192] (solid), $b\bar{b}\tau^+\tau^-$ [193] (dash dot), and $b\bar{b}\gamma\gamma$ [194] (dotted) final states, as a function of $\mathrm{Br}(h \to aa \to 4\tau)$ are shown in black.

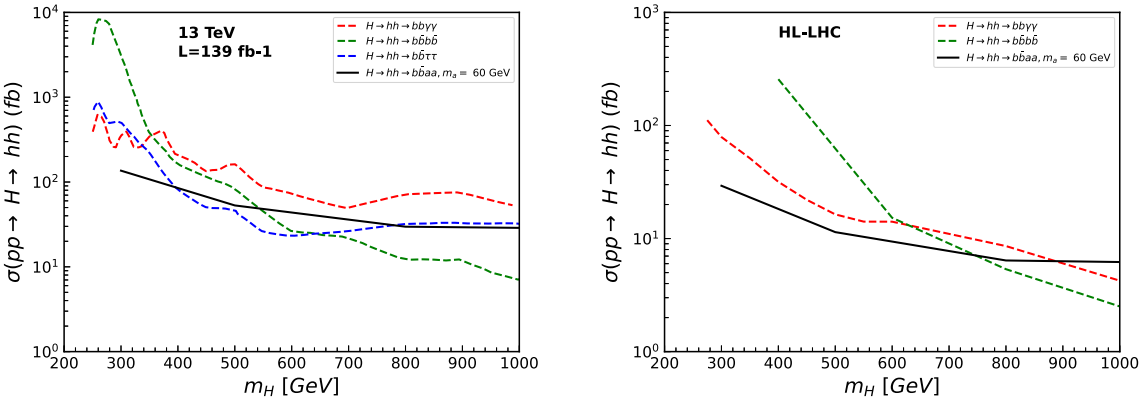

FIG. 15. Left: current upper limits on $\sigma(pp \to H \to hh)$ as a function of m_H from resonant di-Higgs searches in $b\bar{b}b\bar{b}$ [192] (blue), $b\bar{b}\tau^+\tau^-$ [193] (green), and $b\bar{b}\gamma\gamma$ [194] (red) final states. Right: projected upper limits on $\sigma(pp \to H \to hh)$ as a function of m_H from resonant di-Higgs searches in $b\bar{b}b\bar{b}$ (green) and $b\bar{b}\gamma\gamma$ (red) final states at the HL-LHC [131]. The solid-black line in the left and right panels show the sensitivity of the present analysis.

analysis strategy to Sec. II A. We consider the resonant light Higgs pair production, $pp \to H \to aa \to 4\tau$, for two benchmark points, $m_H = 300$, 1000 GeV, with $m_a = 20$, 40, and 60 GeV, as the signal. The relevant background processes are the $gg \to h \to aa \to 4\tau$, the inclusive 4ℓ and $h \to ZZ^* \to 4\ell$ ($\ell = e, \mu, \tau$) processes. Subdominant contributions arise from QCD-QED $4\ell 2\nu$, $4\ell 2b$, $t\bar{t}Z$, $t\bar{t}h$, $t\bar{t}ZZ$, and $t\bar{t}WW$. Table XVI lists the total background yield, the signal

TABLE XVI. Signal efficiency, total background yield, and upper limits at 95% CL on $\sigma(pp \to H \to aa)$ from XGBoost analysis in the $pp \to H \to aa \to 4\tau$ channel at the HL-LHC when $\mathrm{Br}(H \to aa \to 4\tau) = 10\%$.

m_H (GeV)	m_a (GeV)	Total background yield, B	Signal efficiency ($\times 10^{-4}$)	Upper limits on cross section at 95% CL (fb)
300	20	31	12	32
	40	158	146	5.7
	60	270	144	7.6
1000	20	6	1.7	93
	40	24	19	17
	60	86	113	5.5

TABLE XVII. Cross sections of processes: $b\bar{b} \to H$, $t\bar{t} \to H$, and $g\bar{g} \to H$ for $m_H = 500$ GeV and 1000 GeV, as calculated by MadGraph5_aMC@NLO.

	Cross sections at LO (pb)	
Process $\sqrt{s} = 100$ TeV	$m_H = 500$ GeV	$m_H = 1000$ GeV
$b\bar{b} \to H$	0.61	0.055
$t\bar{t} \to H$	24	5.1
$g\bar{g} \to H$	81	5.7

efficiency, and the upper limit on cross-section $\sigma(pp \to H \to aa)$ at 95% CL when $\mathrm{Br}(H \to aa \to 4\tau) = 10\%$.

Although we do not study heavy Higgs production at the FCC-hh, it would be interesting to see how the $t\bar{t}$ and $b\bar{b}$ initiated heavy Higgs production cross sections compare to the ggF cross section at high energy scales. We have used MadGraph5_aMC@NLO for a simple estimation of the cross sections at LO when a heavy Higgs is produced from $b\bar{b}$ and $t\bar{t}$, and how they compare to the heavy Higgs production from ggF. For this, we consider two masses of SM-like heavy Higgs, $m_H = 500$ and 1000 GeV. We use the NNPDF2.3NNLO PDF set [195]. The cross sections are listed in Table XVII.

The LO cross sections of $b\bar{b} \to H$, $t\bar{t} \to H$, and $g\bar{g} \to H$ at $\sqrt{s} = 100$ TeV are 51 (148), 70 (201), 43 (108) times greater than the respective LO cross sections at $\sqrt{s} = 14$ TeV for $m_H = 500$ (1000) GeV. At the 100 TeV collider, the top quark, along with the bottom quark, can be effectively treated as a light particle [196], having a significant contribution to the heavy Higgs production. In such a scenario, a dedicated study involving the $t\bar{t}$ initiated process would be interesting.

VI. SUMMARY

In this paper, we have investigated the prospects for probing the exotic Higgs decay mode $h \to aa \to 4\tau$ in single Higgs and resonant di-Higgs searches at the HL-LHC, and in nonresonant di-Higgs searches at the HL-LHC as well as at the FCC-hh. Searches for exotic Higgs cascade decays to multiple SM particles via new intermediate light (pseudo)scalars are particularly relevant in extending the coverage of BSM models with an extended Higgs sector. We first focused on the ggF $gg \to h \to aa$ and VBF $pp \to (h \to aa)jj$ channels, where the light exotic Higgs boson a subsequently decays to $\tau\bar{\tau}$. We considered five signal benchmarks $m_a = 20$, 30, 40, 50, and 60 GeV and performed a machine-learning-based analysis using the XGBoost algorithm to estimate the projected sensitivity at the HL-LHC. Searches in the ggF-induced single Higgs production channel at the HL-LHC lead to signal significance values of 6.0, 5.4, 5.2, 5.8, and 10.3 in the five signal benchmarks, respectively, for $\mathrm{Br}(h \to aa \to 4\tau) = 0.1\%$. We also derived upper limits on the exotic Higgs branching fraction assuming SM production rates for the Higgs boson, finding that the HL-LHC will be able to probe $\mathrm{Br}(h \to aa \to 4\tau)$ up to $\sim 0.015\%$ at 95% CL for $m_a = 60$ GeV. The VBF production mode yields smaller signal significances at the HL-LHC, the signal significance of 1.5, 2.6, 2.9, 3.1, and 3.7, for $m_a = 20$, 30, 40, 50, and 60 GeV, respectively, mainly due to the smaller cross section. Through searches in the VBF channel, the HL-LHC could exclude $\mathrm{Br}(h \to aa \to 4\tau)$ up to 0.043% at 95% CL for $m_a = 60$ GeV. The combined projected upper limit on $\mathrm{Br}(h \to aa \to 4\tau)$ from searches in the ggF and VBF channels is 0.014% at 95% CL.

Di-Higgs searches in exotic channels provide additional search modes besides the usual SM decay channels. We have analyzed the prospects for probing exotic Higgs decays in the $gg \to hh \to (h \to b\bar{b})(h \to aa \to 4\tau)$ channel at the HL-LHC as well as FCC-hh, for several light scalar masses. The analysis is performed using the traditional cut-and-count approach and the XGBoost algorithm. The cut-based analysis results in the signal significance of 1.1 (24), 2.0 (48), 2.2 (50), 2.3 (54), and 2.5 (59) for the five signal benchmarks, respectively, at the HL-LHC (FCC-hh), for $\mathrm{Br}(h \to aa \to 4\tau) = 10\%$. The XGBoost analysis performs better and leads to a signal significance of 1.4 (35), 2.6 (61), 2.8(67), 2.9(70), and 3.2 (76) for $m_a = 20$, 30, 40, 50, and 50 GeV, respectively, at the HL-LHC (FCC-hh). Overall, the prospects for probing exotic Higgs decays in the di-Higgs channel at the HL-LHC is comparable with the current LHC limits on $\mathrm{Br}(h \to aa \to 4\tau)$ from single Higgs searches [32]. We also investigate the HL-LHC prospects for the Z associated Higgs production channel, $pp \to Zh \to (Z \to b\bar{b})(h \to aa \to 4\tau)$. Searches in this channel furnish comparable results to the nonresonant di-Higgs production.

We finally examine the case of resonant di-Higgs production $pp \to H \to hh \to (h \to b\bar{b})(h \to aa \to 4\tau)$ at the HL-LHC, for several combinations of $\{m_H, m_a\}$. We derive model-independent projected upper limits for $\sigma(pp \to H \to hh)$ as a function of m_H, which are also translated

to the current LHC through luminosity scaling. At the current LHC, the $2b4\tau$ channel considered in the present work performs almost comparably with $4b$, $2b2\tau$, and $2b2\gamma$ channels, provided $\mathrm{Br}(h \to aa \to 4\tau) = 10\%$. The same holds even at the HL-LHC. Current searches put a strong constraint on the resonant di-Higgs production cross section for large masses of heavy Higgs.

This work mainly focused on the 4τ and $2b4\tau$ final states. Possible improvements in the search potential for exotic Higgs decays at future colliders can be expected through combined searches in other final states. Furthermore, the projected sensitivity might benefit through better background modeling, including higher-order signal and background generation effects. Another critical aspect of the HL-LHC and FCC-hh would be to study the implications of systematic uncertainties and devise effective techniques to mitigate their effects. We defer examining these aspects to future work.

ACKNOWLEDGMENTS

A. A. acknowledges partial financial support from the Polish National Science Center under the Beethoven series Grant No. DEC-2016/23/G/ST2/04301. In the final stage of this project, the research of A. A. has received funding from the Norwegian Financial Mechanism for years 2014–2021, Grant No. DEC-2019/34/H/ST2/00707. R. K. B. thanks the U.S. Department of Energy for the financial support under Grant No. DE-SC0016013. The work of Brian Batell is supported by the U.S. Department of Energy under Grant No. DE-SC0007914. Biplob Bhattacherjee and C. B. thank Rhitaja Sengupta and Prabhat Solanki for useful discussion. The work of Zhuoni Qian is supported by the Helmholtz-OCPC fellowship program. The work of Michael Spannowsky is supported by the STFC under Grant No. ST/P001246/1.

APPENDIX A: SUMMARY OF THE GENERATION CUTS AND PRODUCTION CROSS SECTIONS FOR THE SIGNAL AND BACKGROUNDS IN SINGLE HIGGS AND NONRESONANT DI-HIGGS PRODUCTION

TABLE XVIII. Generation level cuts and cross sections for the various backgrounds used in the analyses. The branching ratio for $h \to aa \to 4\tau$ is assumed to be 0.1%.

Process	Signal and backgrounds	Generation-level cuts ($\ell = e^{\pm}, \mu^{\pm}, \tau^{\pm}$) (NA: not applied)	Cross section (fb) at $\sqrt{s} = 14$ TeV
4τ	Signal ($gg \to h \to aa \to 4\tau$)	NA	49.68×10^3
	$gg \to h \to ZZ \to 4l$	NA	10.46
	$4l$	$p_{T,\ell} > 3$ GeV, $\lvert\eta_\ell\rvert < 3.0$, $\Delta R_{\ell\ell} > 0.1$	442.5
	$4l2\nu$	$p_{T,\ell} > 10$ GeV, $\lvert\eta_\ell\rvert < 3.0$, $\Delta R_{\ell\ell} > 0.1$	1.36
	Signal ($pp \to (h \to aa \to 4\tau)jj$)	$p_{T,j} > 20$ GeV, $\lvert\eta_j\rvert < 5.0$, $\Delta R_{jj} > 0.2$, $m_{jj} > 500$ GeV	4.26×10^3
	$4l2j$	$p_{T,j} > 20$ GeV, $p_{T,\ell} > 3$ GeV, $\lvert\eta_j\rvert < 5.0$, $\Delta R_{jj} > 0.2$, $\Delta R_{\ell\ell} > 0.1$, $m_{jj} > 500$ GeV	6.2
	$t\bar{t}h$ ($\geq 3\ell$ final states)	$p_{T,j/b} > 15$ GeV, $p_{T,\ell} > 3$ GeV, $\lvert\eta_j\rvert < 4.0$, $\lvert\eta_{b/\ell}\rvert < 3.0$, $\Delta R_{j,b,\ell} > 0.2$ except $\Delta R_{\ell\ell} > 0.1$, $m_{bb} > 50$ GeV	12.4
	$t\bar{t}Z$, $Z \to \ell\ell$	same as $t\bar{t}h$	29.2
	$4\ell 2b$		1.77
	$t\bar{t}ZZ$ ($\geq 3\ell$ final states)		0.15
	$t\bar{t}WW$ ($\geq 3\ell$ final states)		0.6

TABLE XIX. Generation level cuts and cross sections for the various backgrounds used in the analyses. The branching ratio for $h \to aa \to 4\tau$ is assumed to be 10%.

Process	Signal and backgrounds	Generation-level cuts ($\ell = e^{\pm}, \mu^{\pm}, \tau^{\pm}$) (NA: not applied)	Cross section (fb) at $\sqrt{s} =$ 14 TeV	100 TeV
$b\bar{b}4\tau$	Signal ($pp \to hh \to b\bar{b}aa \to 2b4\tau$)	NA	4.27	142.6
	$t\bar{t}h$ ($\geq 3\ell$ final states)	$p_{T,j/b} > 15$ GeV, $p_{T,\ell} > 3$ GeV, $\lvert\eta_j\rvert < 4.0$, $\lvert\eta_{b/\ell}\rvert < 3.0$, $\Delta R_{j,b,\ell} > 0.2$ except $\Delta R_{\ell\ell} > 0.1$, $m_{bb} > 50$ GeV	12.4	575.7
	$t\bar{t}Z$, $Z \to \ell\ell$	same as $t\bar{t}h$	29.2	1288
	$4\ell 2b$		1.77	31.02
	$t\bar{t}ZZ$ ($\geq 3\ell$ final states)		0.15	7.93
	$t\bar{t}WW$ ($\geq 3\ell$ final states)		0.6	33.2
	$Zh, Z \to b\bar{b}, h \to aa \to 4\tau$	NA	12.64	169.01

APPENDIX B: TRUTH LEVEL TRANSVERSE MOMENTUM DISTRIBUTIONS OF τS IN *VBF* SINGLE HIGGS AND DI-HIGGS PRODUCTION

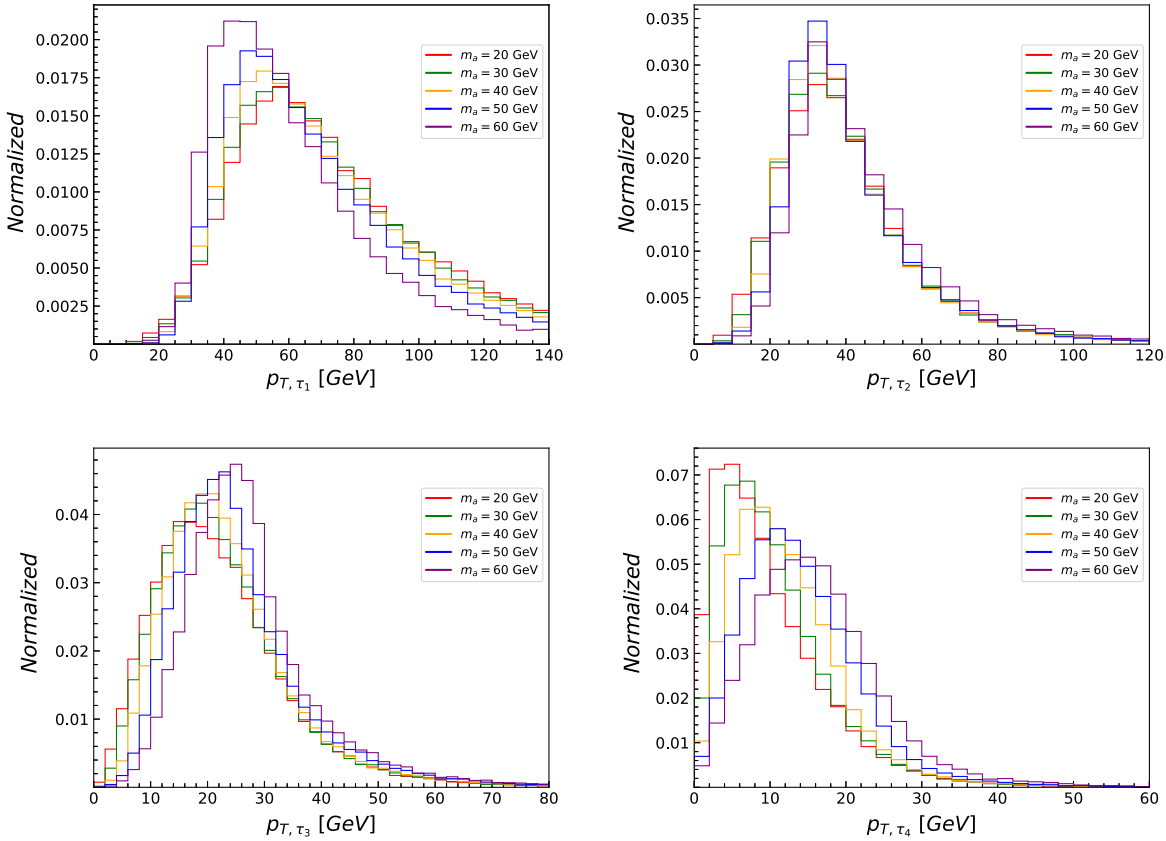

FIG. 16. Distributions for the transverse momentum p_T of the τ leptons at the truth level in the *VBF* production channel $pp \to (h \to aa \to 4\tau)jj$. Here we assume $\sqrt{s} = 14$ TeV LHC.

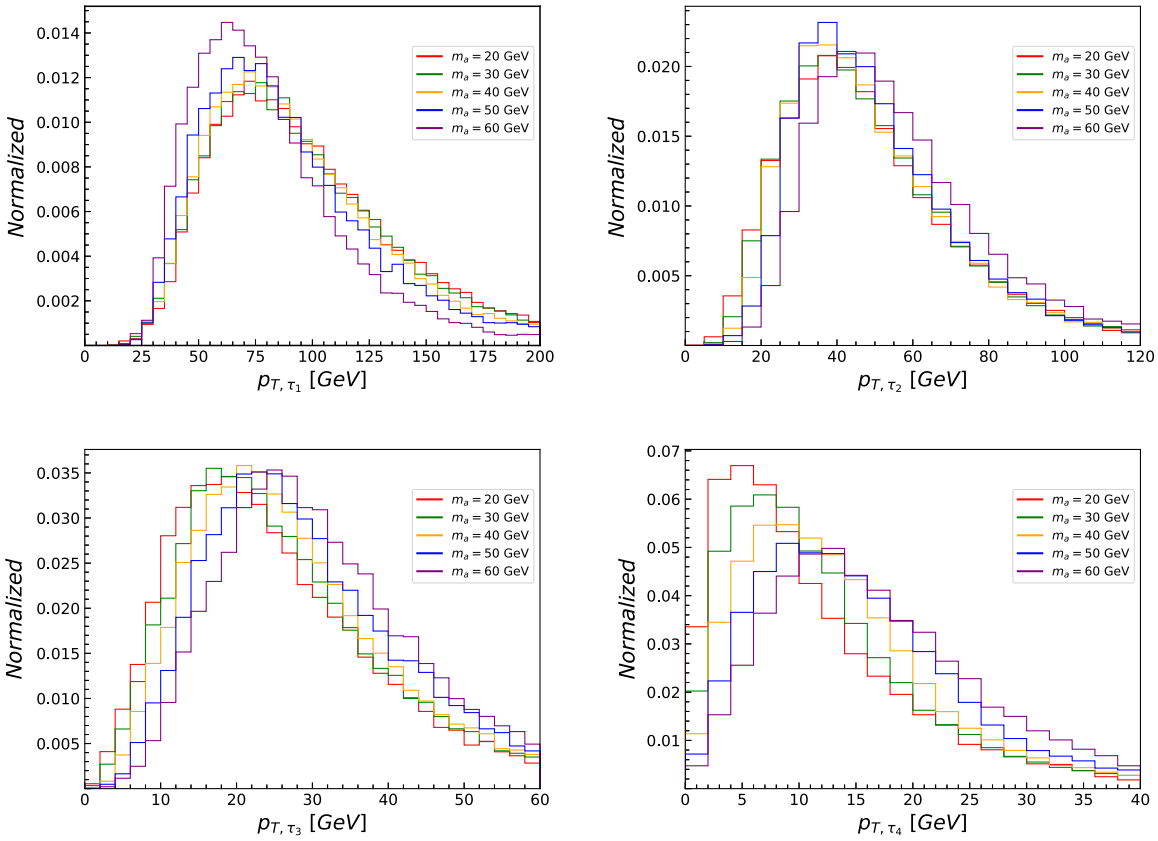

FIG. 17. Distributions for the transverse momentum p_T for the four τ leptons in the nonresonant di-Higgs production channel $pp \to hh \to (h \to b\bar{b})(h \to aa \to 4\tau)$ at the truth level for several exotic scalar masses $m_a = 20$, 30, 40, 50, and 60 GeV. The center of mass energy is fixed at $\sqrt{s} = 14$ TeV.

APPENDIX C: NORMALIZED DISTRIBUTION FOR KINEMATIC OBSERVABLES IN NONRESONANT DI-HIGGS PRODUCTION AT THE HL-LHC AND FCC-HH

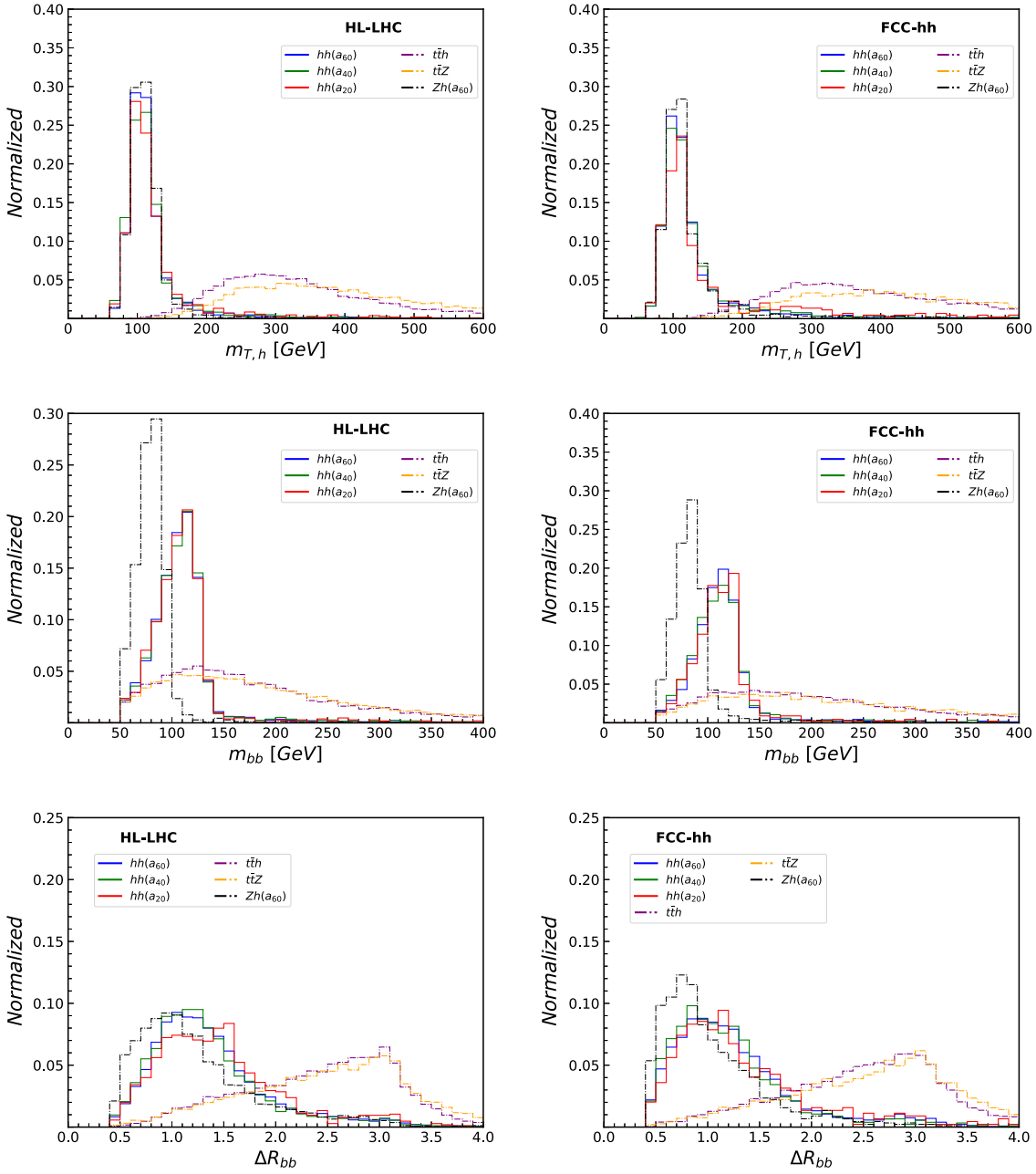

FIG. 18. Distributions of $m_{T,h}$, m_{bb}, and ΔR_{bb} for signal benchmarks $m_a = 20, 40, 60$ GeV, and dominant backgrounds, in the $pp \to hh \to (h \to b\bar{b})(h \to aa \to 4\tau)$ channel. The left and right panels show the distributions at $\sqrt{s} = 14$ and 100 TeV, respectively.

APPENDIX D: XGBOOST ANALYSIS OF NONRESONANT DI-HIGGS PRODUCTION AT FCC-HH WITH JET RADIUS $R = 0.4$

We list the results for the case where $R = 0.4$ is used to reconstruct jets at the FCC-hh. Compared with Table XI, the signal efficiency in the case of $R = 0.3$ jets is 1.2–1.8 times more than in the case of $R = 0.4$ jets.

TABLE XX. Signal and background yields, and signal significance, at the FCC-hh from XGBoost analysis in the $pp \to hh \to (h \to b\bar{b})(h \to aa \to 4\tau)$ channel. The results shown here have been derived for Br $(h \to aa \to 4\tau) \sim 10\%$.

$\sqrt{s}$ (TeV)	m_a (GeV)	Total background yield, B	Signal efficiency ($\times 10^{-4}$)	Signal yield, S	Significance (5% systematic)
100	20	514	2.2	965	25 (21)
	30	959	6.7	2866	46 (37)
	40	993	9.9	4240	59 (48)
	50	1046	10	4383	59 (48)
	60	1146	12	5108	64 (52)

[1] ATLAS Collaboration, A combination of measurements of Higgs boson production and decay using up to 139 fb^{-1} of proton–proton collision data at $\sqrt{s} = 13$ TeV collected with the ATLAS experiment, Technical Report No. ATLAS-CONF-2020-027, CERN, Geneva, 2020.

[2] D. Curtin *et al.*, Exotic decays of the 125 GeV Higgs boson, Phys. Rev. D **90**, 075004 (2014).

[3] M. Cepeda, S. Gori, V. M. Outschoorn, and J. Shelton, Exotic Higgs decays, Annu. Rev. Nucl. Part. Sci. **72**, 119 (2022).

[4] V. Silveira and A. Zee, Scalar phantoms, Phys. Lett. **161B**, 136 (1985).

[5] C. P. Burgess, M. Pospelov, and T. ter Veldhuis, The minimal model of nonbaryonic dark matter: A singlet scalar, Nucl. Phys. **B619**, 709 (2001).

[6] P. Draper, T. Liu, C. E. M. Wagner, L.-T. Wang, and H. Zhang, Dark light Higgs, Phys. Rev. Lett. **106**, 121805 (2011).

[7] C. Englert, T. Plehn, D. Zerwas, and P. M. Zerwas, Exploring the Higgs portal, Phys. Lett. B **703**, 298 (2011).

[8] B. Bhattacherjee, S. Matsumoto, S. Mukhopadhyay, and M. M. Nojiri, Phenomenology of light fermionic asymmetric dark matter, J. High Energy Phys. 10 (2013) 032.

[9] T. Robens and T. Stefaniak, Status of the Higgs singlet extension of the standard model after LHC run 1, Eur. Phys. J. C **75**, 104 (2015).

[10] T. Robens and T. Stefaniak, LHC benchmark scenarios for the real Higgs singlet extension of the standard model, Eur. Phys. J. C **76**, 268 (2016).

[11] T. Robens, T. Stefaniak, and J. Wittbrodt, Two-real-scalar-singlet extension of the SM: LHC phenomenology and benchmark scenarios, Eur. Phys. J. C **80**, 151 (2020).

[12] M. Bauer, M. Neubert, and A. Thamm, Collider probes of axion-like particles, J. High Energy Phys. 12 (2017) 044.

[13] A. Alves, A. G. Dias, and D. D. Lopes, Jets and photons spectroscopy of Higgs-ALP interactions, J. High Energy Phys. 10 (2021) 012.

[14] U. Ellwanger, C. Hugonie, and A. M. Teixeira, The next-to-minimal supersymmetric standard model, Phys. Rep. **496**, 1 (2010).

[15] H. Nilles, M. Srednicki, and D. Wyler, Weak interaction breakdown induced by supergravity, Phys. Lett. **120B**, 346 (1983).

[16] J. Ellis, J. F. Gunion, H. E. Haber, L. Roszkowski, and F. Zwirner, Higgs bosons in a nonminimal supersymmetric model, Phys. Rev. D **39**, 844 (1989).

[17] M. Aaboud *et al.* (ATLAS Collaboration), Search for the Higgs boson produced in association with a vector boson and decaying into two spin-zero particles in the $H \to aa \to 4b$ channel in pp collisions at $\sqrt{s} = 13$ TeV with the ATLAS detector, J. High Energy Phys. 10 (2018) 031.

[18] G. Aad *et al.* (ATLAS Collaboration), Search for Higgs boson decays into two new low-mass spin-0 particles in the $4b$ channel with the ATLAS detector using pp collisions at $\sqrt{s} = 13$ TeV, Phys. Rev. D **102**, 112006 (2020).

[19] A. Sirunyan, A. Tumasyan, W. Adam, F. Ambrogi, E. Asilar, T. Bergauer *et al.*, Search for an exotic decay of the Higgs boson to a pair of light pseudoscalars in the final state with two b quarks and two τ leptons in proton–proton collisions at $\sqrt{s} = 13$ tev, Phys. Lett. B **785**, 462 (2018).

[20] M. Aaboud *et al.* (ATLAS Collaboration), Search for Higgs boson decays into a pair of light bosons in the $bb\mu\mu$ final state in pp collision at $\sqrt{s} = 13$ TeV with the ATLAS detector, Phys. Lett. B **790**, 1 (2019).

[21] A. M. Sirunyan *et al.* (CMS Collaboration), Search for an exotic decay of the Higgs boson to a pair of light pseudoscalars in the final state with two muons and two b quarks in pp collisions at 13 TeV, Phys. Lett. B **795**, 398 (2019).

[22] G. Aad *et al.* (ATLAS Collaboration), Search for Higgs boson decays into a pair of pseudoscalar particles in the $bb\mu\mu$ final state with the ATLAS detector in pp collisions at $\sqrt{s} = 13$ TeV, Phys. Rev. D **105**, 012006 (2022).

[23] A. Sirunyan, A. Tumasyan, W. Adam, F. Ambrogi, E. Asilar, T. Bergauer *et al.*, A search for pair production of new light bosons decaying into muons in proton-proton collisions at 13 tev, Phys. Lett. B **796**, 131 (2019).

[24] M. Aaboud *et al.* (ATLAS Collaboration), Search for Higgs boson decays to beyond-the-standard-model light bosons in four-lepton events with the ATLAS detector at $\sqrt{s} = 13$ TeV, J. High Energy Phys. 06 (2018) 166.

[25] A. M. Sirunyan, A. Tumasyan, W. Adam, F. Ambrogi, T. Bergauer, M. Dragicevic *et al.*, Search for a light pseudoscalar Higgs boson in the boosted $\mu\mu\tau\tau$ final state in proton-proton collisions at $\sqrt{s} = 13$ tev, J. High Energy Phys. 08 (2020) 139.

[26] A. Sirunyan, A. Tumasyan, W. Adam, F. Ambrogi, E. Asilar, T. Bergauer *et al.*, Search for light pseudoscalar boson pairs produced from decays of the 125 GeV Higgs boson in final states with two muons and two nearby tracks in pp collisions at $\sqrt{s} = 13$ tev, Phys. Lett. B **800**, 135087 (2020).

[27] A. M. Sirunyan *et al.* (CMS Collaboration), Search for an exotic decay of the Higgs boson to a pair of light pseudoscalars in the final state of two muons and two τ leptons in proton-proton collisions at $\sqrt{s} = 13$ TeV, J. High Energy Phys. 11 (**2018**) 018.

[28] V. Khachatryan *et al.* (CMS Collaboration), Search for light bosons in decays of the 125 GeV Higgs boson in proton-proton collisions at $\sqrt{s} = 8$ TeV, J. High Energy Phys. 10 (2017) 076.

[29] G. Aad *et al.* (ATLAS Collaboration), Search for Higgs bosons decaying to aa in the $\mu\mu\tau\tau$ final state in pp collisions at $\sqrt{s} = 8$ TeV with the ATLAS experiment, Phys. Rev. D **92**, 052002 (2015).

[30] G. Aad *et al.* (ATLAS Collaboration), Search for new phenomena in events with at least three photons collected in pp collisions at $\sqrt{s} = 8$ TeV with the ATLAS detector, Eur. Phys. J. C **76**, 210 (2016).

[31] M. Aaboud *et al.* (ATLAS Collaboration), Search for Higgs boson decays into pairs of light (pseudo)scalar particles in the $\gamma\gamma jj$ final state in pp collisions at $\sqrt{s} =$ 13 TeV with the ATLAS detector, Phys. Lett. B **782**, 750 (2018).

[32] H. Cai, Search for exotic Higgs boson decays to four leptons with the ATLAS detector, Ph.D. thesis, Illinois U., Urbana, 2020.

[33] CMS Collaboration, A search for anomalous production of events with three or more leptons using 9.2 fb^{-1} of $\sqrt{s} =$ 8 TeV CMS data, Technical Report No. CMS-PAS-SUS-12-026, CERN, Geneva, 2012.

[34] CMS Collaboration, Search for RPV SUSY in the four-lepton final state, Technical Report No. CMS-PAS-SUS-13-010, CERN, Geneva, 2013.

[35] S. Banerjee, B. Batell, and M. Spannowsky, Invisible decays in Higgs boson pair production, Phys. Rev. D **95**, 035009 (2017).

[36] E. Arganda, J. L. Díaz-Cruz, N. Mileo, R. A. Morales, and A. Szynkman, Search strategies for pair production of heavy Higgs bosons decaying invisibly at the LHC, Nucl. Phys. **B929**, 171 (2018).

[37] A. Alves, T. Ghosh, and F. S. Queiroz, Dark and bright signatures of di-Higgs boson production, Phys. Rev. D **100**, 036012 (2019).

[38] A. Abada *et al.* (FCC Collaboration), FCC Physics Opportunities: Future Circular Collider Conceptual Design Report Volume 1, Eur. Phys. J. C **79**, 474 (2019).

[39] S. Dawson, S. Dittmaier, and M. Spira, Neutral Higgs boson pair production at hadron colliders: QCD corrections, Phys. Rev. D **58**, 115012 (1998).

[40] S. Borowka, N. Greiner, G. Heinrich, S. Jones, M. Kerner, J. Schlenk, U. Schubert, and T. Zirke, Higgs boson pair production in gluon fusion at next-to-leading order with full top-quark mass dependence, Phys. Rev. Lett. **117**, 012001 (2016).

[41] J. Baglio, F. Campanario, S. Glaus, M. Mühlleitner, M. Spira, and J. Streicher, Gluon fusion into Higgs pairs at NLO QCD and the top mass scheme, Eur. Phys. J. C **79**, 459 (2019).

[42] D. de Florian and J. Mazzitelli, Higgs boson pair production at next-to-next-to-leading order in QCD, Phys. Rev. Lett. **111**, 201801 (2013).

[43] D. Y. Shao, C. S. Li, H. T. Li, and J. Wang, Threshold resummation effects in Higgs boson pair production at the LHC, J. High Energy Phys. 07 (2013) 169.

[44] D. de Florian and J. Mazzitelli, Higgs pair production at next-to-next-to-leading logarithmic accuracy at the LHC, J. High Energy Phys. 09 (2015) 053.

[45] M. Grazzini, G. Heinrich, S. Jones, S. Kallweit, M. Kerner, J. M. Lindert, and J. Mazzitelli, Higgs boson pair production at NNLO with top quark mass effects, J. High Energy Phys. 05 (2018) 059.

[46] J. Baglio, F. Campanario, S. Glaus, M. Mühlleitner, J. Ronca, M. Spira, and Juraj Streicher, Higgs-pair production via gluon fusion at hadron colliders: NLO QCD corrections, J. High Energy Phys. 04 (2020) 181.

[47] M. Aaboud *et al.* (ATLAS Collaboration), Search for pair production of Higgs bosons in the $b\bar{b}b\bar{b}$ final state using proton-proton collisions at $\sqrt{s} = 13$ TeV with the ATLAS detector, J. High Energy Phys. 01 (2019) 030.

[48] M. Aaboud *et al.* (ATLAS Collaboration), Search for resonant and non-resonant Higgs boson pair production in the $b\bar{b}\tau^+\tau^-$ decay channel in pp collisions at $\sqrt{s} =$ 13 TeV with the ATLAS detector, Phys. Rev. Lett. **121**, 191801 (2018).

[49] A. M. Sirunyan *et al.* (CMS Collaboration), Search for Higgs boson pair production in events with two bottom quarks and two tau leptons in proton–proton collisions at $\sqrt{s} = 13$ TeV, Phys. Lett. B **778**, 101 (2018).

[50] M. Aaboud *et al.* (ATLAS Collaboration), Search for Higgs boson pair production in the $\gamma\gamma b\bar{b}$ final state with 13 TeV pp collision data collected by the ATLAS experiment, J. High Energy Phys. 11 (2018) 040.

[51] CMS Collaboration, Search for Higgs boson pair production in the final state containing two photons and two bottom quarks in proton-proton collisions at $\sqrt{s} = 13$ TeV.

[52] M. Aaboud *et al.* (ATLAS Collaboration), Search for Higgs boson pair production in the $b\bar{b}WW^*$ decay mode

at $\sqrt{s} = 13$ TeV with the ATLAS detector, J. High Energy Phys. 04 (2019) 092.
[53] M. Aaboud *et al.* (ATLAS Collaboration), Search for Higgs boson pair production in the $\gamma\gamma WW^*$ channel using pp collision data recorded at $\sqrt{s} = 13$ TeV with the ATLAS detector, Eur. Phys. J. C **78**, 1007 (2018).
[54] M. Aaboud *et al.* (ATLAS Collaboration), Search for Higgs boson pair production in the $WW^{(*)}WW^{(*)}$ decay channel using ATLAS data recorded at $\sqrt{s} = 13$ TeV, J. High Energy Phys. 05 (**2019**) 124.
[55] D. de Florian, C. Grojean, F. Maltoni, C. Mariotti, A. Nikitenko, M. Pieri *et al.* (LHCHiggsCrossSection WorkingGroup Collaboration), *Handbook of LHC Higgs Cross Sections: 4. Deciphering the Nature of the Higgs Sector*, CERN Yellow Reports: Monographs (CERN, Geneva, 2017), 10.23731/CYRM-2017-002.
[56] G. Durieux, G. Durieux, M. McCullough, M. McCullough, E. Salvioni, and E. Salvioni, Charting the Higgs self-coupling boundaries, J. High Energy Phys. 12 (2022) 148.
[57] A. Tumasyan *et al.* (CMS Collaboration), A portrait of the Higgs boson by the CMS experiment ten years after the discovery., Nature (London) **607**, 60 (2022).
[58] G. Aad *et al.* (ATLAS Collaboration), Constraints on the Higgs boson self-coupling from single- and double-Higgs production with the ATLAS detector using pp collisions at s = 13 TeV, Phys. Lett. B **843**, 137745 (2023).
[59] M. J. Dolan, C. Englert, and M. Spannowsky, Higgs self-coupling measurements at the LHC, J. High Energy Phys. 10 (2012) 112.
[60] J. H. Kim, K. Kong, K. T. Matchev, and M. Park, Probing the triple Higgs self-interaction at the large hadron collider, Phys. Rev. Lett. **122**, 091801 (2019).
[61] J. H. Kim, M. Kim, K. Kong, K. T. Matchev, and M. Park, Portraying double Higgs at the large hadron collider, J. High Energy Phys. 09 (**2019**) 047.
[62] A. J. Barr, M. J. Dolan, C. Englert, and M. Spannowsky, Di-Higgs final states augMT2ed—selecting hh events at the high luminosity LHC, Phys. Lett. B **728**, 308 (2014).
[63] V. Barger, L. L. Everett, C. B. Jackson, and G. Shaughnessy, Higgs-pair production and measurement of the triscalar coupling at LHC(8,14), Phys. Lett. B **728**, 433 (2014).
[64] F. Kling, T. Plehn, and P. Schichtel, Maximizing the significance in Higgs boson pair analyses, Phys. Rev. D **95**, 035026 (2017).
[65] A. Alves, T. Ghosh, and K. Sinha, Can we discover double Higgs production at the LHC?, Phys. Rev. D **96**, 035022 (2017).
[66] A. Adhikary, S. Banerjee, R. K. Barman, B. Bhattacherjee, and S. Niyogi, Revisiting the non-resonant Higgs pair production at the HL-LHC, J. High Energy Phys. 07 (2018) 116.
[67] J. Amacker *et al.*, Higgs self-coupling measurements using deep learning and jet substructure in the $b\bar{b}b\bar{b}$ final state, J. High Energy Phys. 12 (**2020**) 115.
[68] M. Abdughani, D. Wang, L. Wu, J. M. Yang, and J. Zhao, Probing triple Higgs coupling with machine learning at the LHC, Phys. Rev. D **104**, 056003 (2021).
[69] G. Heinrich, S. Jones, M. Kerner, G. Luisoni, and L. Scyboz, Probing the trilinear Higgs boson coupling in di-Higgs production at NLO QCD including parton shower effects, J. High Energy Phys. 06 (2019) 066.
[70] E. Arganda, C. Garcia-Garcia, and M. J. Herrero, Probing the Higgs self-coupling through double Higgs production in vector boson scattering at the LHC, Nucl. Phys. **B945**, 114687 (2019).
[71] J. Chang, K. Cheung, J. S. Lee, C.-T. Lu, and J. Park, Higgs-boson-pair production $H(\to b\bar{b})H(\to\gamma\gamma)$ from gluon fusion at the HL-LHC and HL-100 TeV hadron collider, Phys. Rev. D **100**, 096001 (2019).
[72] Q.-H. Cao, Y. Liu, and B. Yan, Measuring trilinear Higgs coupling in WHH and ZHH productions at the high-luminosity LHC, Phys. Rev. D **95**, 073006 (2017).
[73] M. L. Mangano, G. Ortona, and M. Selvaggi, Measuring the Higgs self-coupling via Higgs-pair production at a 100 TeV p-p collider, Eur. Phys. J. C **80**, 1030 (2020).
[74] S. Banerjee, F. Krauss, and M. Spannowsky, Revisiting the $t\bar{t}hh$ channel at the FCC-hh, Phys. Rev. D **100**, 073012 (2019).
[75] S. Banerjee, C. Englert, M. L. Mangano, M. Selvaggi, and M. Spannowsky, hh + jet production at 100 TeV, Eur. Phys. J. C **78**, 322 (2018).
[76] W. Bizoń, U. Haisch, and L. Rottoli, Constraints on the quartic Higgs self-coupling from double-Higgs production at future hadron colliders, J. High Energy Phys. 10 (2019) 267.
[77] D. Gonçalves, T. Han, F. Kling, T. Plehn, and M. Takeuchi, Higgs boson pair production at future hadron colliders: From kinematics to dynamics, Phys. Rev. D **97**, 113004 (2018).
[78] A. J. Barr, M. J. Dolan, C. Englert, D. E. Ferreira de Lima, and M. Spannowsky, Higgs self-coupling measurements at a 100 TeV hadron collider, J. High Energy Phys. 02 (2015) 016.
[79] R. Contino *et al.*, Physics at a 100 TeV pp collider: Higgs and EW symmetry breaking studies, arXiv:1606.09408.
[80] J. Park, J. Chang, K. Cheung, and J. S. Lee, Measuring the trilinear Higgs boson self–coupling at the 100 TeV hadron collider via multivariate analysis, Phys. Rev. D **102**, 073002 (2020).
[81] A. Adhikary, R. K. Barman, and B. Bhattacherjee, Prospects of non-resonant di-Higgs searches and Higgs boson self-coupling measurement at the HE-LHC using machine learning techniques, J. High Energy Phys. 12 (2020) 179.
[82] J.-J. Liu, W.-G. Ma, G. Li, R.-Y. Zhang, and H.-S. Hou, Higgs boson pair production in the little Higgs model at hadron collider, Phys. Rev. D **70**, 015001 (2004).
[83] C. O. Dib, R. Rosenfeld, and A. Zerwekh, Double Higgs production and quadratic divergence cancellation in little Higgs models with T parity, J. High Energy Phys. 05 (2006) 074.
[84] A. Pierce, J. Thaler, and L.-T. Wang, Disentangling dimension six operators through Di-Higgs boson production, J. High Energy Phys. 05 (2007) 070.
[85] L. Wang, W. Wang, J. M. Yang, and H. Zhang, Higgs-pair production in littlest Higgs model with T-parity, Phys. Rev. D **76**, 017702 (2007).
[86] S. Kanemura and K. Tsumura, Effects of the anomalous Higgs couplings on the Higgs boson production at the large hadron collider, Eur. Phys. J. C **63**, 11 (2009).

[87] R. Contino, C. Grojean, M. Moretti, F. Piccinini, and R. Rattazzi, Strong double Higgs production at the LHC, J. High Energy Phys. 05 (**2010**) 089.
[88] R. Grober and M. Muhlleitner, Composite Higgs boson pair production at the LHC, J. High Energy Phys. 06 (2011) 020.
[89] H. Sun, Y.-J. Zhou, and H. Chen, Constraints on large-extra-dimensions model through 125-GeV Higgs pair production at the LHC, Eur. Phys. J. C **72**, 2011 (2012).
[90] R. Contino, M. Ghezzi, M. Moretti, G. Panico, F. Piccinini, and A. Wulzer, Anomalous couplings in double Higgs production, J. High Energy Phys. 08 (2012) 154.
[91] G. D. Kribs and A. Martin, Enhanced di-Higgs production through light colored scalars, Phys. Rev. D **86**, 095023 (2012).
[92] M. J. Dolan, C. Englert, and M. Spannowsky, New physics in LHC Higgs boson pair production, Phys. Rev. D **87**, 055002 (2013).
[93] K. Nishiwaki, S. Niyogi, and A. Shivaji, *ttH* anomalous coupling in double Higgs production, J. High Energy Phys. 04 (2014) 011.
[94] U. Ellwanger, Higgs pair production in the NMSSM at the LHC, J. High Energy Phys. 08 (2013) 077.
[95] J. Cao, Z. Heng, L. Shang, P. Wan, and J. M. Yang, Pair production of a 125 GeV Higgs boson in MSSM and NMSSM at the LHC, J. High Energy Phys. 04 (2013) 134.
[96] S. Dawson, E. Furlan, and I. Lewis, Unravelling an extended quark sector through multiple Higgs production?, Phys. Rev. D **87**, 014007 (2013).
[97] J. M. No and M. Ramsey-Musolf, Probing the Higgs portal at the LHC through resonant di-Higgs production, Phys. Rev. D **89**, 095031 (2014).
[98] F. Goertz, A. Papaefstathiou, L. L. Yang, and J. Zurita, Higgs boson pair production in the $D = 6$ extension of the SM, J. High Energy Phys. 04 (2015) 167.
[99] N. Liu, S. Hu, B. Yang, and J. Han, Impact of top-Higgs couplings on Di-Higgs production at future colliders, J. High Energy Phys. 01 (**2015**) 008.
[100] C.-R. Chen and I. Low, Double take on new physics in double Higgs boson production, Phys. Rev. D **90**, 013018 (2014).
[101] J. Baglio, O. Eberhardt, U. Nierste, and M. Wiebusch, Benchmarks for Higgs pair production and heavy Higgs boson searches in the two-Higgs-doublet model of type II, Phys. Rev. D **90**, 015008 (2014).
[102] B. Hespel, D. Lopez-Val, and E. Vryonidou, Higgs pair production via gluon fusion in the Two-Higgs-Doublet Model, J. High Energy Phys. 09 (2014) 124.
[103] V. Barger, L. L. Everett, C. B. Jackson, A. D. Peterson, and G. Shaughnessy, New physics in resonant production of Higgs boson pairs, Phys. Rev. Lett. **114**, 011801 (2015).
[104] S. Dawson, A. Ismail, and I. Low, What's in the loop? The anatomy of double Higgs production, Phys. Rev. D **91**, 115008 (2015).
[105] A. Azatov, R. Contino, G. Panico, and M. Son, Effective field theory analysis of double Higgs boson production via gluon fusion, Phys. Rev. D **92**, 035001 (2015).
[106] L.-C. Lü, C. Du, Y. Fang, H.-J. He, and H. Zhang, Searching heavier Higgs boson via di-Higgs production at LHC Run-2, Phys. Lett. B **755**, 509 (2016).
[107] C.-T. Lu, J. Chang, K. Cheung, and J. S. Lee, An exploratory study of Higgs-boson pair production, J. High Energy Phys. 08 (2015) 133.
[108] A. Carvalho, M. Dall'Osso, T. Dorigo, F. Goertz, C. A. Gottardo, and M. Tosi, Higgs pair production: Choosing benchmarks with cluster analysis, J. High Energy Phys. 04 (2016) 126.
[109] Q.-H. Cao, B. Yan, D.-M. Zhang, and H. Zhang, Resolving the degeneracy in single Higgs production with Higgs pair production, Phys. Lett. B **752**, 285 (2016).
[110] R. Costa, M. Mühlleitner, M. O. P. Sampaio, and R. Santos, Singlet extensions of the standard model at LHC run 2: Benchmarks and comparison with the NMSSM, J. High Energy Phys. 06 (2016) 034.
[111] B. Batell, M. McCullough, D. Stolarski, and C. B. Verhaaren, Putting a stop to di-Higgs modifications, J. High Energy Phys. 09 (**2015**) 216.
[112] Q.-H. Cao, G. Li, B. Yan, D.-M. Zhang, and H. Zhang, Double Higgs production at the 14 TeV LHC and the 100 TeV pp-collider, Phys. Rev. D **96**, 095031 (2017).
[113] A. V. Kotwal, M. J. Ramsey-Musolf, J. M. No, and P. Winslow, Singlet-catalyzed electroweak phase transitions in the 100 TeV frontier, Phys. Rev. D **94**, 035022 (2016).
[114] R. Grober, M. Muhlleitner, and M. Spira, Signs of composite Higgs pair production at next-to-leading order, J. High Energy Phys. 06 (2016) 080.
[115] L. Bian and N. Chen, Higgs pair productions in the *CP*-violating two-Higgs-doublet model, J. High Energy Phys. 09 (2016) 069.
[116] A. Crivellin, M. Ghezzi, and M. Procura, Effective field theory with two Higgs doublets, J. High Energy Phys. 09 (2016) 160.
[117] M. Gorbahn and U. Haisch, Indirect probes of the trilinear Higgs coupling: $gg \to h$ and $h \to \gamma\gamma$, J. High Energy Phys. 10 (2016) 094.
[118] A. Carvalho, M. Dall'Osso, P. De Castro Manzano, T. Dorigo, F. Goertz, M. Gouzevich *et al.*, Analytical parametrization and shape classification of anomalous HH production in the EFT approach, Technical Report No. ATL-PHYS-PUB-2015-045, arXiv:1608.06578.
[119] P. Huang, A. Joglekar, M. Li, and C. E. M. Wagner, Corrections to di-Higgs boson production with light stops and modified Higgs couplings, Phys. Rev. D **97**, 075001 (2018).
[120] K. Nakamura, K. Nishiwaki, K.-y. Oda, S. C. Park, and Y. Yamamoto, Di-Higgs enhancement by neutral scalar as probe of new colored sector, Eur. Phys. J. C **77**, 273 (2017).
[121] Y. Gao and N. A. Neill, Probing exotic triple Higgs couplings for almost inert Higgs bosons at the LHC, J. High Energy Phys. 05 (**2020**) 087.
[122] P. Huang and Y. H. Ng, Di-Higgs production in SUSY models at the LHC, Eur. Phys. J. Plus **135**, 660 (2020).
[123] D. Barducci, K. Mimasu, J. No, C. Vernieri, and J. Zurita, Enlarging the scope of resonant di-Higgs searches: Hunting for Higgs-to-Higgs cascades in $4b$ final states at the LHC and future colliders, J. High Energy Phys. 02 (2020) 002.
[124] P. Basler, S. Dawson, C. Englert, and M. Mühlleitner, Di-Higgs boson peaks and top valleys: Interference effects

in Higgs sector extensions, Phys. Rev. D **101**, 015019 (2020).
[125] A. Alves, D. Gonçalves, T. Ghosh, H.-K. Guo, and K. Sinha, Di-Higgs production in the 4*b* channel and gravitational wave complementarity, J. High Energy Phys. 03 (2020) 053.
[126] C. Englert and J. Jaeckel, Probing the symmetric Higgs portal with di-Higgs boson production, Phys. Rev. D **100**, 095017 (2019).
[127] M. Bauer, M. Carena, and A. Carmona, Higgs pair production as a signal of enhanced Yukawa couplings, Phys. Rev. Lett. **121**, 021801 (2018).
[128] K. Babu and S. Jana, Enhanced di-Higgs production in the two Higgs doublet model, J. High Energy Phys. 02 (2019) 193.
[129] P. Basler, S. Dawson, C. Englert, and M. Mühlleitner, Showcasing HH production: Benchmarks for the LHC and HL-LHC, Phys. Rev. D **99**, 055048 (2019).
[130] A. Alves, T. Ghosh, H.-K. Guo, K. Sinha, and D. Vagie, Collider and gravitational wave complementarity in exploring the singlet extension of the standard model, J. High Energy Phys. 04 (2019) 052.
[131] A. Adhikary, S. Banerjee, R. Kumar Barman, and B. Bhattacherjee, Resonant heavy Higgs searches at the HL-LHC, J. High Energy Phys. 09 (2019) 068.
[132] S. Borowka, C. Duhr, F. Maltoni, D. Pagani, A. Shivaji, and X. Zhao, Probing the scalar potential via double Higgs boson production at hadron colliders, J. High Energy Phys. 04 (2019) 016.
[133] N. Chen, C. Du, Y. Wu, and X.-J. Xu, Further study of the global minimum constraint on the two-Higgs-doublet models: LHC searches for heavy Higgs bosons, Phys. Rev. D **99**, 035011 (2019).
[134] A. Alves, T. Ghosh, H.-K. Guo, and K. Sinha, Resonant di-Higgs production at gravitational wave benchmarks: A collider study using machine learning, J. High Energy Phys. 12 (2018) 070.
[135] G. Buchalla, M. Capozi, A. Celis, G. Heinrich, and L. Scyboz, Higgs boson pair production in non-linear effective field theory with full m_t-dependence at NLO QCD, J. High Energy Phys. 09 (**2018**) 057.
[136] Z. Heng, X. Gong, and H. Zhou, Pair production of Higgs boson in NMSSM at the LHC with the next-to-lightest *CP*-even Higgs boson being SM-like, Chin. Phys. C **42**, 073103 (2018).
[137] J. H. Kim, Y. Sakaki, and M. Son, Combined analysis of double Higgs production via gluon fusion at the HL-LHC in the effective field theory approach, Phys. Rev. D **98**, 015016 (2018).
[138] M. Flores, C. Gross, J. S. Kim, O. Lebedev, and S. Mondal, Multi-Higgs probes of the dark sector, Phys. Rev. D **102**, 015004 (2020).
[139] C. Englert, D. J. Miller, and D. D. Smaranda, Phenomenology of GUT-inspired gauge-Higgs unification, Phys. Lett. B **802**, 135261 (2020).
[140] J. Alison *et al.*, Higgs boson potential at colliders: Status and perspectives, Rev. Phys. **5**, 100045 (2020).
[141] L. Alasfar, R. Corral Lopez, and R. Gröber, Probing Higgs couplings to light quarks via Higgs pair production, J. High Energy Phys. 11 (2019) 088.
[142] M. Capozi and G. Heinrich, Exploring anomalous couplings in Higgs boson pair production through shape analysis, J. High Energy Phys. 03 (2020) 091.
[143] G. Li, L.-X. Xu, B. Yan, and C.-P. Yuan, Resolving the degeneracy in top quark Yukawa coupling with Higgs pair production, Phys. Lett. B **800**, 135070 (2020).
[144] K. Cheung, A. Jueid, C.-T. Lu, J. Song, and Y. W. Yoon, Disentangling new physics effects on non-resonant Higgs boson pair production from gluon fusion, Phys. Rev. D **103**, 015019 (2021).
[145] T. Kon, T. Nagura, T. Ueda, and K. Yagyu, Double Higgs boson production at e^+e^- colliders in the two-Higgs-doublet model, Phys. Rev. D **99**, 095027 (2019).
[146] A. Arhrib, R. Benbrik, M. El Kacimi, L. Rahili, and S. Semlali, Extended Higgs sector of 2HDM with real singlet facing LHC data, Eur. Phys. J. C **80**, 13 (2020).
[147] H. Bahl, P. Bechtle, S. Heinemeyer, S. Liebler, T. Stefaniak, and G. Weiglein, HL-LHC and ILC sensitivities in the hunt for heavy Higgs bosons, Eur. Phys. J. C **80**, 916 (2020).
[148] R. K. Barman, C. Englert, D. Gonçalves, and M. Spannowsky, Di-Higgs resonance searches in weak boson fusion, Phys. Rev. D **102**, 055014 (2020).
[149] K. Cheung, Y.-L. Chung, and S.-C. Hsu, Sensitivity on two-Higgs-doublet models from Higgs-pair production via $b\bar{b}b\bar{b}$ final state, Phys. Rev. D **106**, 095015 (2022).
[150] M. A. Arroyo-Ureña, A. Chakraborty, J. L. Díaz-Cruz, D. K. Ghosh, N. Khan, and S. Moretti, Higgs pair production at the LHC through the flavon, Phys. Rev. D **108**, 095026 (2023).
[151] A. Bhaskar, D. Das, B. De, S. Mitra, A. K. Nayak, and C. Neeraj, Leptoquark-assisted singlet-mediated di-Higgs production at the LHC, Phys. Lett. B **833**, 137341 (2022).
[152] S. Kanemura, M. Kikuchi, and K. Yagyu, Next-to-leading order corrections to decays of the heavier *CP*-even Higgs boson in the two Higgs doublet model, Nucl. Phys. **B983**, 115906 (2022).
[153] https://twiki.cern.ch/twiki/bin/view/LHCPhysics/CERNYellowReportPageAt14TeV.
[154] G. Aad *et al.* (ATLAS Collaboration), Measurements of Higgs bosons decaying to bottom quarks from vector boson fusion production with the ATLAS experiment at $\sqrt{s} = 13$ TeV, Eur. Phys. J. C **81**, 537 (2021).
[155] G. Aad *et al.* (ATLAS Collaboration), Constraints on Higgs boson production with large transverse momentum using $H \to b\bar{b}$ decays in the ATLAS detector, Phys. Rev. D **105**, 092003 (2022).
[156] ATLAS Collaboration, Measurement of the properties of Higgs boson production at $\sqrt{s} = 13$ TeV in the $H \to \gamma\gamma$ channel using 139 fb^{-1} of pp collision data with the ATLAS experiment, J. High Energy Phys. 07 (2023) 088.
[157] ATLAS Collaboration, Measurement of the total and differential Higgs boson production cross-sections at $\sqrt{s} =$ 13 TeV with the ATLAS detector by combining the $H \to ZZ^* \to 4\ell$ and $H \to \gamma\gamma$ decay channels, J. High Energy Phys. 05 (2023) 028.
[158] G. Aad *et al.* (ATLAS Collaboration), Measurements of Higgs boson production cross-sections in the $H \to \tau^+\tau^-$ decay channel in pp collisions at $\sqrt{s} = 13$ TeV with the ATLAS detector, J. High Energy Phys. 08 (2022) 175.

[159] ATLAS Collaboration, Measurement of the Higgs boson mass in the $H \to ZZ^* \to 4\ell$ decay channel using 139 fb^{-1} of $\sqrt{s} = 13$ TeV pp collisions recorded by the ATLAS detector at the LHC, Phys. Lett. B **843**, 137880 (2023).

[160] ATLAS Collaboration, Measurements of Higgs boson production by gluon—gluon fusion and vector-boson fusion using $H \to WW^* \to e\nu\mu\nu$ decays in pp collisions at $\sqrt{s} = 13$ TeV with the ATLAS detector, Phys. Rev. D **108**, 032005 (2023).

[161] G. Aad *et al.* (ATLAS Collaboration), Constraints on Higgs boson properties using $WW^*(\to e\nu\mu\nu)jj$ production in 36.1 fb^{-1} of $\sqrt{s} = 13$ TeV pp collisions with the ATLAS detector, Eur. Phys. J. C **82**, 622 (2022).

[162] G. Aad *et al.* (ATLAS Collaboration), A search for the dimuon decay of the standard model Higgs boson with the ATLAS detector, Phys. Lett. B **812**, 135980 (2021).

[163] J. Alwall, R. Frederix, S. Frixione, V. Hirschi, F. Maltoni, O. Mattelaer, H.-S. Shao, T. Stelzer, P. Torrielli, and M. Zaro, The automated computation of tree-level and next-to-leading order differential cross sections, and their matching to parton shower simulations, J. High Energy Phys. 07 (2014) 079.

[164] T. Sjostrand, L. Lonnblad, and S. Mrenna, PYTHIA 6.2: Physics and manual, arXiv:hep-ph/0108264.

[165] T. Sjöstrand, S. Ask, J. R. Christiansen, R. Corke, N. Desai, P. Ilten, S. Mrenna, S. Prestel, C. O. Rasmussen, and P. Z. Skands, An Introduction to PYTHIA 8.2, Comput. Phys. Commun. **191**, 159 (2015).

[166] M. Cacciari, G. P. Salam, and G. Soyez, The anti-k(t) jet clustering algorithm, J. High Energy Phys. 04 (2008) 063.

[167] M. Cacciari, G. P. Salam, and G. Soyez, FastJet user manual, Eur. Phys. J. C **72**, 1896 (2012).

[168] J. de Favereau, C. Delaere, P. Demin, A. Giammanco, V. Lemaître, A. Mertens, and M. Selvaggi (DELPHES 3 Collaboration), DELPHES 3, A modular framework for fast simulation of a generic collider experiment, J. High Energy Phys. 02 (2014) 057.

[169] A. M. Sirunyan *et al.* (CMS Collaboration), Identification of heavy-flavour jets with the CMS detector in pp collisions at 13 TeV, J. Instrum. **13**, P05011 (2018).

[170] CMS Collaboration, Performance of reconstruction and identification of tau leptons in their decays to hadrons and tau neutrino in LHC Run-2, Technical Report CMS-PAS-TAU-16-002, CERN, Geneva, 2016.

[171] T. Chen and C. Guestrin, XGBoost: A scalable tree boosting system, in *Proceedings of the 22nd ACM SIGKDD International Conference on Knowledge Discovery and Data Mining*, KDD '16, (ACM, New York, NY, USA, 2016), pp. 785–794.

[172] S. Lundberg and S.-I. Lee, A unified approach to interpreting model predictions, arXiv:1705.07874.

[173] S. M. Lundberg, G. G. Erion, and S.-I. Lee, Consistent individualized feature attribution for tree ensembles, arXiv:1802.03888.

[174] L. S. Shapley, *17. A Value for n-Person Games* (Princeton University Press, Princeton, NJ, 2016), pp. 307–318.

[175] A. S. Cornell, W. Doorsamy, B. Fuks, G. Harmsen, and L. Mason, Boosted decision trees in the era of new physics: A smuon analysis case study, J. High Energy Phys. 04 (2022) 015.

[176] D. Alvestad, N. Fomin, J. Kersten, S. Maeland, and I. Strümke, Beyond cuts in small signal scenarios—enhanced sneutrino detectability using machine learning, Eur. Phys. J. C **83**, 379 (2023).

[177] C. Grojean, A. Paul, and Z. Qian, Resurrecting $b\bar{b}h$ with kinematic shapes, J. High Energy Phys. 04 (2021) 139.

[178] A. Tumasyan *et al.* (CMS Collaboration), Evidence for WW/WZ vector boson scattering in the decay channel $\ell\nu$qq produced in association with two jets in proton-proton collisions at s = 13 TeV, Phys. Lett. B **834**, 137438 (2022).

[179] C. Grojean, A. Paul, Z. Qian, and I. Strümke, Lessons on interpretable machine learning from particle physics, Nat. Rev. Phys. **4**, 284 (2022).

[180] G. Aad *et al.* (ATLAS Collaboration), A detailed map of Higgs boson interactions by the ATLAS experiment ten years after the discovery, Nature (London) **607**, 52 (2022).

[181] ATLAS Collaboration, Reconstruction, energy calibration, and identification of hadronically decaying tau leptons in the ATLAS experiment for run-2 of the LHC, Technical Report, CERN, Geneva, 2015.

[182] A. Tumasyan, W. Adam, J. Andrejkovic, T. Bergauer, S. Chatterjee, M. Dragicevic *et al.*, Identification of hadronic tau lepton decays using a deep neural network, J. Instrum. **17**, P07023 (2022).

[183] A. Elagin, P. Murat, A. Pranko, and A. Safonov, A new mass reconstruction technique for resonances decaying to di-tau, Nucl. Instrum. Methods Phys. Res., Sect. A **654**, 481 (2011).

[184] M. Aaboud *et al.* (ATLAS Collaboration), Search for pair production of Higgs bosons in the $b\bar{b}b\bar{b}$ final state using proton-proton collisions at $\sqrt{s} = 13$ TeV with the ATLAS detector, J. High Energy Phys. 01 (2019) 030.

[185] C. G. Lester and D. J. Summers, Measuring masses of semiinvisibly decaying particles pair produced at hadron colliders, Phys. Lett. B **463**, 99 (1999).

[186] A. Barr, C. Lester, and P. Stephens, m(T2): The truth behind the glamour, J. Phys. G **29**, 2343 (2003).

[187] M. Selvaggi, A Delphes parameterisation of the FCC-hh detector, Technical Report No. CERN-FCC-PHYS-2020-0003, CERN, Geneva, 2020.

[188] U. Ellwanger, C. Hugonie, and A. M. Teixeira, The next-to-minimal supersymmetric standard model, Phys. Rep. **496**, 1 (2010).

[189] A. Djouadi, U. Ellwanger, and A. M. Teixeira, Phenomenology of the constrained NMSSM, J. High Energy Phys. 04 (2009) 031.

[190] C.-Y. Chen, M. Freid, and M. Sher, Next-to-minimal two Higgs doublet model, Phys. Rev. D **89**, 075009 (2014).

[191] P. Zyla *et al.* (Particle Data Group Collaboration), Review of particle physics, Prog. Theor. Exp. Phys. **2020**, 083C01 (2020).

[192] ATLAS Collaboration, Search for resonant pair production of Higgs bosons in the $b\bar{b}b\bar{b}$ final state using pp collisions at $\sqrt{s} = 13$ TeV with the ATLAS detector, Technical Report No. ATLAS-CONF-2021-035, CERN, Geneva, 2021.

[193] ATLAS Collaboration, Search for resonant and non-resonant Higgs boson pair production in the $b\bar{b}\tau^+\tau^-$ decay channel using 13 TeV pp collision data from the ATLAS detector, Technical Report No. ATLAS-CONF-2021-030, CERN, Geneva, 2021.

[194] ATLAS Collaboration, Search for Higgs boson pair production in the two bottom quarks plus two photons final state in pp collisions at $\sqrt{s} = 13$ TeV with the ATLAS detector, Technical Report No. ATLAS-CONF-2021-016, CERN, Geneva, 2021.

[195] R. D. Ball *et al.*, Parton distributions with LHC data, Nucl. Phys. **B867**, 244 (2013).

[196] M. L. Mangano *et al.*, Physics at a 100 TeV pp collider: Standard model processes, Report No. CERN-TH-2016-112, 2016.